

Bulk synthesis of Zn_3WN_4 via solid-state metathesis

Christopher L. Rom¹, Shaun O'Donnell^{1,2}, Kayla Huang^{1,3}, Ryan A. Klein^{1,4}, Morgan J. Kramer^{4,5}, Rebecca W. Smaha¹, Andriy Zakutayev^{1,*}

¹ Materials, Chemical, and Computational Science, National Renewable Energy Laboratory, Golden, CO, 80401, USA

² Department of Chemistry, Colorado State University, Fort Collins, CO, 80523, USA

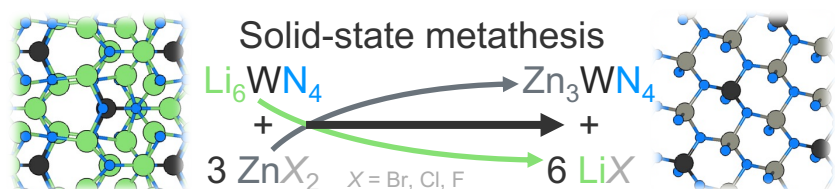
³ University of Illinois Urbana-Champaign, Champaign, IL, 61801, USA

⁴ Center for Neutron Research, National Institute of Standards and Technology, Gaithersburg, MD, 20899, USA

⁵ Department of Chemistry, Southern Methodist University, Dallas, TX, 75275 USA

* Corresponding author: andriy.zakutayev@nrel.gov

TOC figure



Abstract

Ternary nitrides are of growing technological importance, with applications as semiconductors, catalysts, and magnetic materials; however, new synthetic tools are needed to advance materials discovery efforts. Here, we show that Zn_3WN_4 can be synthesized via metathesis reactions between Li_6WN_4 and ZnX_2 ($X = \text{Br}, \text{Cl}, \text{F}$). *In situ* synchrotron powder X-ray diffraction and differential scanning calorimetry show that the reaction onset is correlated with the ZnX_2 melting point and that product purity is inversely correlated with the reaction's exothermicity. High resolution synchrotron powder X-ray diffraction measurements show that this bulk synthesis produces a structure with substantial cation ordering, as opposed to the disordered structure initially discovered via thin film sputtering. Diffuse reflectance spectroscopy reveals that Zn_3WN_4 powders exhibit two optical absorption onsets at ~ 2.5 eV and ~ 4.0 eV, indicating wide-bandgap semiconducting behavior and suggesting a small amount of structural disorder. We hypothesize that this synthesis strategy is generalizable because many potential Li- M -N precursors are available for synthesizing new ternary nitride materials (where M is a metal). This work introduces a promising synthesis strategy that will accelerate the discovery of novel functional ternary nitrides and other currently inaccessible materials.

Introduction

Ternary nitrides are a promising class of semiconducting materials,^[1] yet relatively few are known. This dearth of nitrides is primarily due to the synthetic challenges of realizing these materials from elemental metal (or binary) precursors and dinitrogen gas.^[1–4] Molecular (di)nitrogen, N_2 , is highly stable, and high temperatures are needed to break the strong $\text{N}\equiv\text{N}$ triple bond (945 kJ/mol). High temperatures are also needed to drive diffusion, as nitrides tend to have high cohesive energies (i.e., strong M -N bonds) and slow diffusion.^[5–7] Moreover, entropic penalties disfavor nitride incorporation in solids. Finding a synthesis temperature that is hot enough for reactivity but cool enough to avoid decomposition is therefore challenging. Adding to the difficulty, O_2 is more reactive towards most metals than N_2 , so syntheses must be conducted in rigorously air-free conditions to avoid the formation of oxide impurities. Consequently, the number of known ternary nitrides lags behind the ternary oxides by an order of magnitude.^[1–4] Developing new synthesis methods will help narrow this disparity, and in doing so, discover new materials upon which improved technologies can be built.

Zn-containing ternary nitrides epitomize the promising applications and synthetic challenges of this class of materials. Fully nitridized compounds like ZnSnN_2 and Zn_3WN_4 (with metals in the highest oxidation state) are of interest as semiconductors for their high earth abundance and tunable bandgaps (spanning ca. 1 eV for ZnSnN_2 to 3.6 eV for Zn_3WN_4).^[8,9] However, the bulk syntheses techniques that have been reported for Zn- M -N phases are limited to traditional ceramic methods (i.e., metals + N_2 or NH_3 at high temperatures) or high-pressure solid state metathesis reactions (e.g., $2 \text{Li}_3\text{N} + \text{ZnF}_2 + \text{SnF}_4 \rightarrow \text{ZnSnN}_2 + 6 \text{LiF}$).^[10,11] These bulk methods have only produced fully nitridized phases when M is a main group element (i.e., LiZnN , Ca_2ZnN_2 , Sr_2ZnN_2 , Ba_2ZnN_2 , ZnSiN_2 , ZnGeN_2 , ZnSnN_2).^[6,8–18] When transition metals are used in bulk syntheses, they tend to form sub-nitrides: e.g., $\text{Ti}_3\text{ZnN}_{0.5}$, $\text{V}_3\text{Zn}_2\text{N}$, Ti_2ZnN , Mn_3ZnN , and Fe_3ZnN .^[19–24] The nitrogen-poor nature of these materials stems from the challenges described above (i.e., N_2 stability, slow diffusion). Synthesizing fully-nitridized Zn- M -N (where M is a transition metal) in bulk would advance technologies in which thin film nitrides have already shown promise, like photoelectrochemical energy conversion (ZnTiN_2),^[25] transparent conducting oxides (ZnZrN_2),^[26]

and non-linear optics (Zn_3WN_4).^[27] However, no bulk synthesis methods have been reported for fully nitridized Zn-*M*-N ternaries.

Synthesizing Zn-*M*-N ternary nitrides via traditional methods is difficult. Many transition metals are highly refractory, meaning high temperatures would likely be needed for interdiffusion of reactants. However, Zn has a low melting point (419 °C) and a relatively low boiling point (907 °C), meaning that high temperatures would volatilize Zn away from the other metal unless special measures were taken (e.g., high pressure, closed vessels). Forming binary nitrides to use as precursors instead of metals is also challenging: Zn (like other late-transition metals) does not react with N_2 at elevated temperatures, so Zn_3N_2 must be synthesized under ammonia.^[28] And as noted in thin film work, fully nitridized transition metal Zn-*M*-N phases have low decomposition temperatures on the order of 600-700 °C.^[3,25,26,29] These challenges mean that bulk synthesis of Zn-*M*-N from the elements or binaries would likely proceed only at low temperatures and extremely slowly, unless special high-pressure methods were employed (e.g., ammonothermal synthesis,^[11] diamond anvil cell synthesis,^[30] etc.).

Metathesis reactions (i.e., ion exchange reactions) are one promising way to circumvent the challenge of diffusion in the solid state.^[31] To synthesize nitrides, this strategy starts with one nitrogen-containing precursor and one halide precursor, rather than elements or binary nitrides. The balanced reaction targets the desired phase along with a byproduct (often a halide salt). The formation of this byproduct provides a large thermodynamic driving force for the reaction and (ideally) can be washed away post-reaction. For example, Kaner et al. showed that mixing Li_3N with metal chlorides would produce LiCl in explosively exothermic metathesis reactions that yielded a range of binary nitrides^[32–42] and some ternary nitrides.^[43,44] Alternatively, less exothermic reactions can be conducted with greater synthetic control,^[45–49] including low-temperature topotactic reactions (T_{rxn} ca. 200–400 °C).^[50–52] As for Zn-*M*-N compounds, ZnSnN_2 and ZnSiN_2 have been made using high pressure metathesis reactions, where the pressure is necessary to avoid gaseous N_2 loss.^[10,18] This strategy is well known for “turning down the heat” in solid state synthesis^[53] but is underutilized for synthesizing nitrides.

Here, we synthesize Zn_3WN_4 via a near-topotactic ion exchange reaction between Li_6WN_4 and ZnX_2 ($X = \text{F}, \text{Cl}, \text{Br}$) at 300 °C and ambient pressure. *In situ* synchrotron powder X-ray diffraction (SPXRD) paired with differential scanning calorimetry measurements reveal the reaction pathway taken by this reaction and show that using a ZnBr_2 precursor is preferable over the fluoride or chloride analogs. High resolution SPXRD measurements indicate that the Zn_3WN_4 product is a mostly cation-ordered structure in space group $Pmn2_1$. We report some preliminary properties characterizations for Zn_3WN_4 , revealing an optical absorption onsets near 2.5 eV and 4.0 eV, as well as paramagnetism consistent with some degree of disorder and off-stoichiometry. The reaction is near-topotactic, in that the structures of the Li_6WN_4 precursor and the Zn_3WN_4 product are related by a shift in anion layers but the $[\text{WN}_4]$ tetrahedral unit is preserved. Using this synthesis approach, we also synthesized Zn_3MoN_4 , albeit with lower levels of purity in our un-optimized reactions. This work demonstrates the viability of Li-*M*-N phases as metathesis precursors to synthesize other ternary nitride compounds, expanding the toolkit for materials discovery.

Results and Discussion

In situ SPXRD measurements

Zn_3WN_4 was successfully synthesized via metathesis (ion exchange) reactions. The net reaction is:



In situ variable temperature SPXRD measurements reveal that Li_6WN_4 directly converts to Zn_3WN_4 without intermediate crystalline phases or solid solution behavior as a function of temperature (Figure 1, Figures S2, S3). However, the halide precursor exerts an influence on the reaction kinetics and thermodynamics, which ultimately impact the reaction pathway and final product purity.

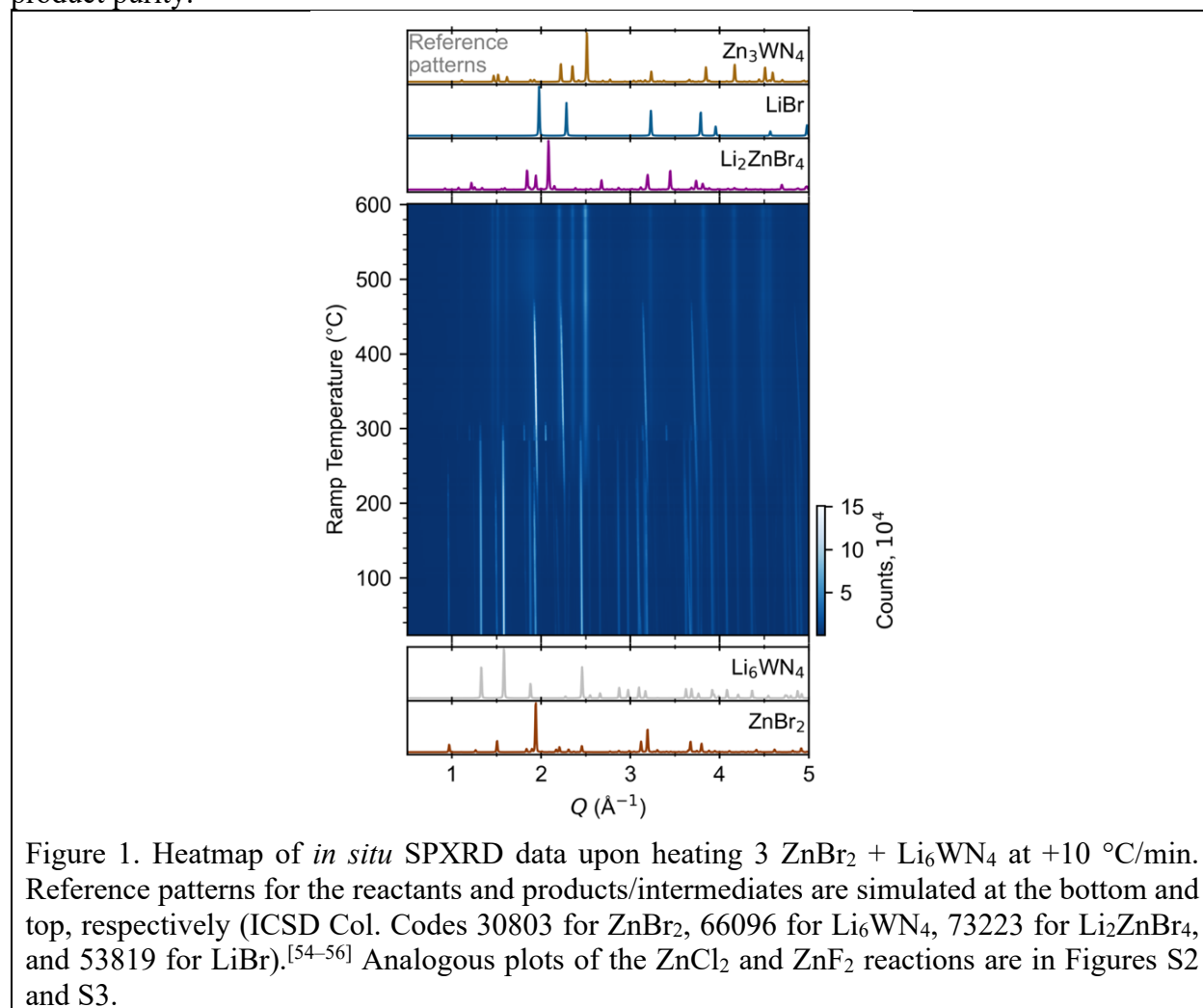
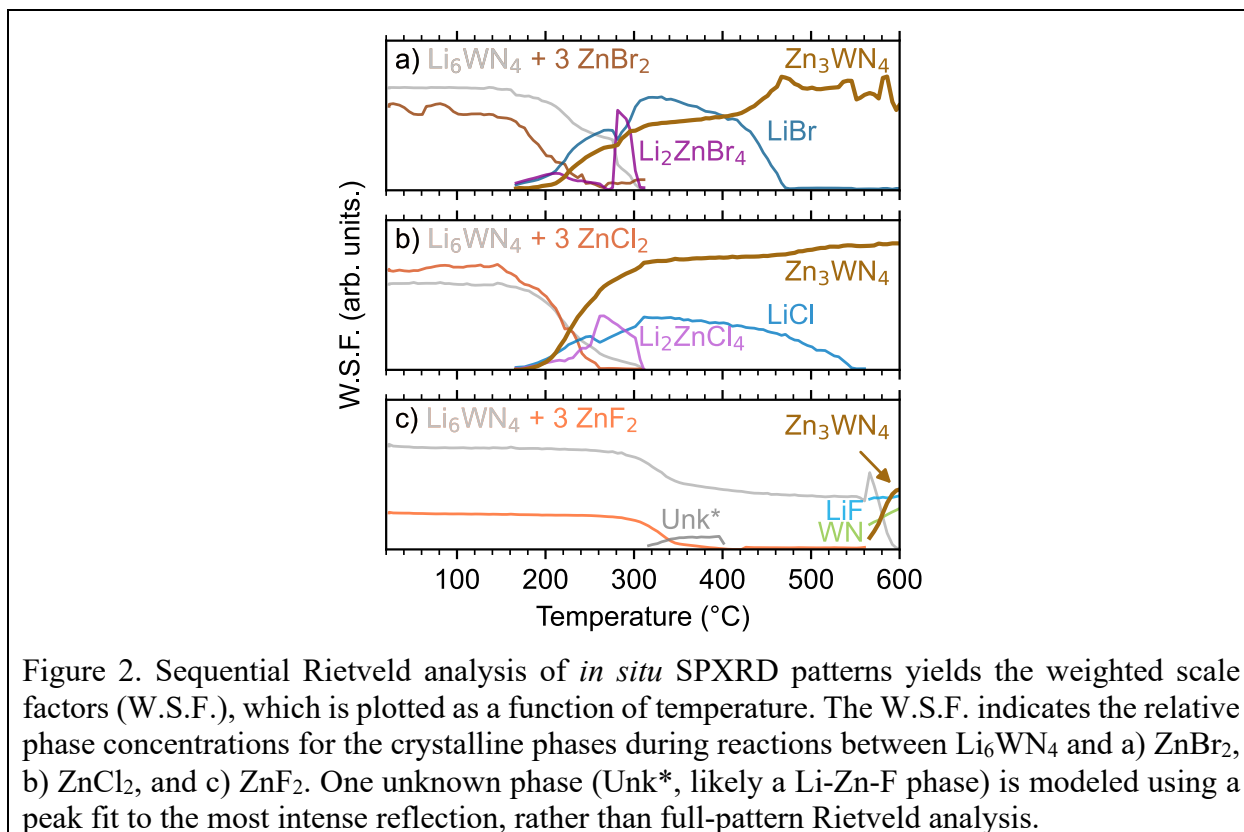


Figure 1. Heatmap of *in situ* SPXRD data upon heating $3 \text{ZnBr}_2 + \text{Li}_6\text{WN}_4$ at $+10 \text{ }^\circ\text{C/min}$. Reference patterns for the reactants and products/intermediates are simulated at the bottom and top, respectively (ICSD Col. Codes 30803 for ZnBr_2 , 66096 for Li_6WN_4 , 73223 for Li_2ZnBr_4 , and 53819 for LiBr).^[54–56] Analogous plots of the ZnCl_2 and ZnF_2 reactions are in Figures S2 and S3.

In situ SPXRD measurements reveal that the reaction pathway proceeds without intermediate nitrides between Li_6WN_4 and Zn_3WN_4 . Here, $X = \text{Br}$ is shown as an example; subsequent examination revealed that it leads to the most phase pure product. The reaction of $\text{Li}_6\text{WN}_4 + 3 \text{ZnBr}_2 \rightarrow \text{Zn}_3\text{WN}_4 + 6 \text{LiBr}$ initiates near $170 \text{ }^\circ\text{C}$ and proceeds to completion within the 14 minutes of ramp time up to $310 \text{ }^\circ\text{C}$ (Figure 1). Near $170 \text{ }^\circ\text{C}$, the Bragg peaks arising from crystalline Li_6WN_4 and ZnBr_2 begin to gradually decline in intensity. Shortly thereafter, new sets of Bragg peaks that can be indexed to LiBr , Li_2ZnBr_4 , and Zn_3WN_4 begin growing in intensity in the

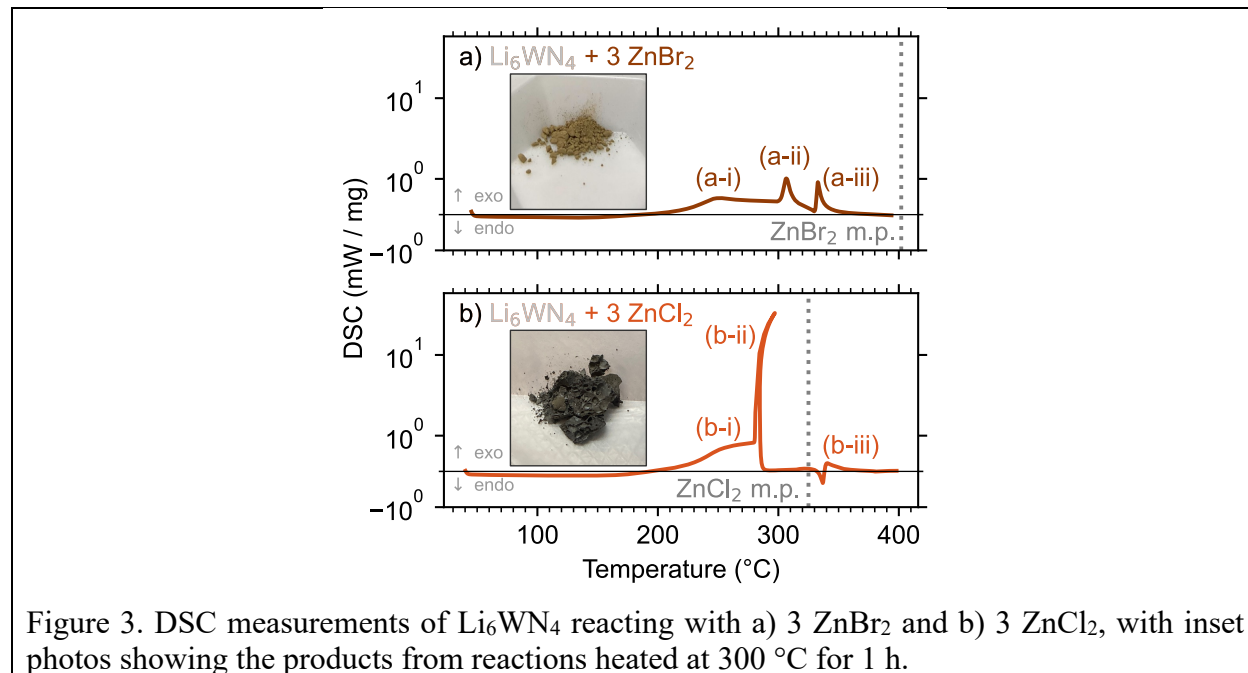
patterns. The Bragg peaks corresponding to Li_2ZnBr_4 gradually decrease in intensity between 210 °C and 270 °C, increase dramatically in intensity at 275 °C, and then disappear entirely at 305 °C. Such fluctuations may stem from crystal nucleation and growth within the capillary, especially given the small spot size of the synchrotron X-ray beam, possibly combined with crystallite motion in a liquid-like medium. Diffraction images show spotty diffraction patterns, consistent with crystallite growth. These data indicate that the synthesis proceeds directly via $\text{Li}_6\text{WN}_4 + 3 \text{ZnBr}_2 \rightarrow \text{Zn}_3\text{WN}_4 + 6 \text{LiBr}$. While this process occurs, an incidental reaction between the metal halides also occurs: $2 \text{LiBr} + \text{ZnBr}_2 \rightarrow \text{Li}_2\text{ZnBr}_4$. We do not observe signs of a crystalline theoretically-predicted $\text{LiZn}_4\text{W}_2\text{N}_7$ structure,^[57] although this does not rule out the presence or synthesizability of such a phase. Similar trends are noted with the ZnCl_2 and ZnF_2 reactions (Figures S2, S3), as shown by sequential Rietveld analysis (Figure 2).



Sequential Rietveld analysis of *in situ* variable temperature SPXRD measurements of the $\text{Li}_6\text{WN}_4 + 3 \text{ZnX}_2$ reactions shows that the ZnBr_2 and ZnCl_2 reactions initiate at much lower temperatures than the ZnF_2 reaction (Figure 2). For both the ZnBr_2 and ZnCl_2 reactions (Figure 2a,b), the concentrations of the precursor phases start decreasing near 170 °C, followed shortly thereafter by Zn_3WN_4 and LiX formation and growth. Ternary halides Li_2ZnBr_4 and Li_2ZnCl_4 are short-lived, incidental intermediates. In contrast, in the fluoride reaction, the concentration of ZnF_2 does not begin declining until approximately 300 °C (Figure 2c). The concomitant decrease in Li_6WN_4 concentration suggests reactivity, but neither Zn_3WN_4 nor LiF are detected in our data. Instead, very weak reflections for an unknown phase appear in the data (labeled as Unk*). This phase may be a Li-Zn-F ternary, but it does not index to any known ternary fluoride unit cells, including the reported Li_2ZnF_4 phase.^[58] An amorphous phase is likely present in the 400 to 570 °C region, given

the decrease in precursor peaks and lack of new intermediate peaks. Zn_3WN_4 and LiF crystallize above 570 °C, along with a rocksalt phase (fit with WN, but the material may be a $(\text{Zn},\text{W})\text{N}_x$ phase as observed with the Mo-based system, Figure S11). We did not study the ZnF_2 reactions further, given that phase-pure Zn_3WN_4 did not crystallize and given the challenge associated with washing away LiF from the product. Instead, we focus on ZnBr_2 and ZnCl_2 reactions.

DSC measurements



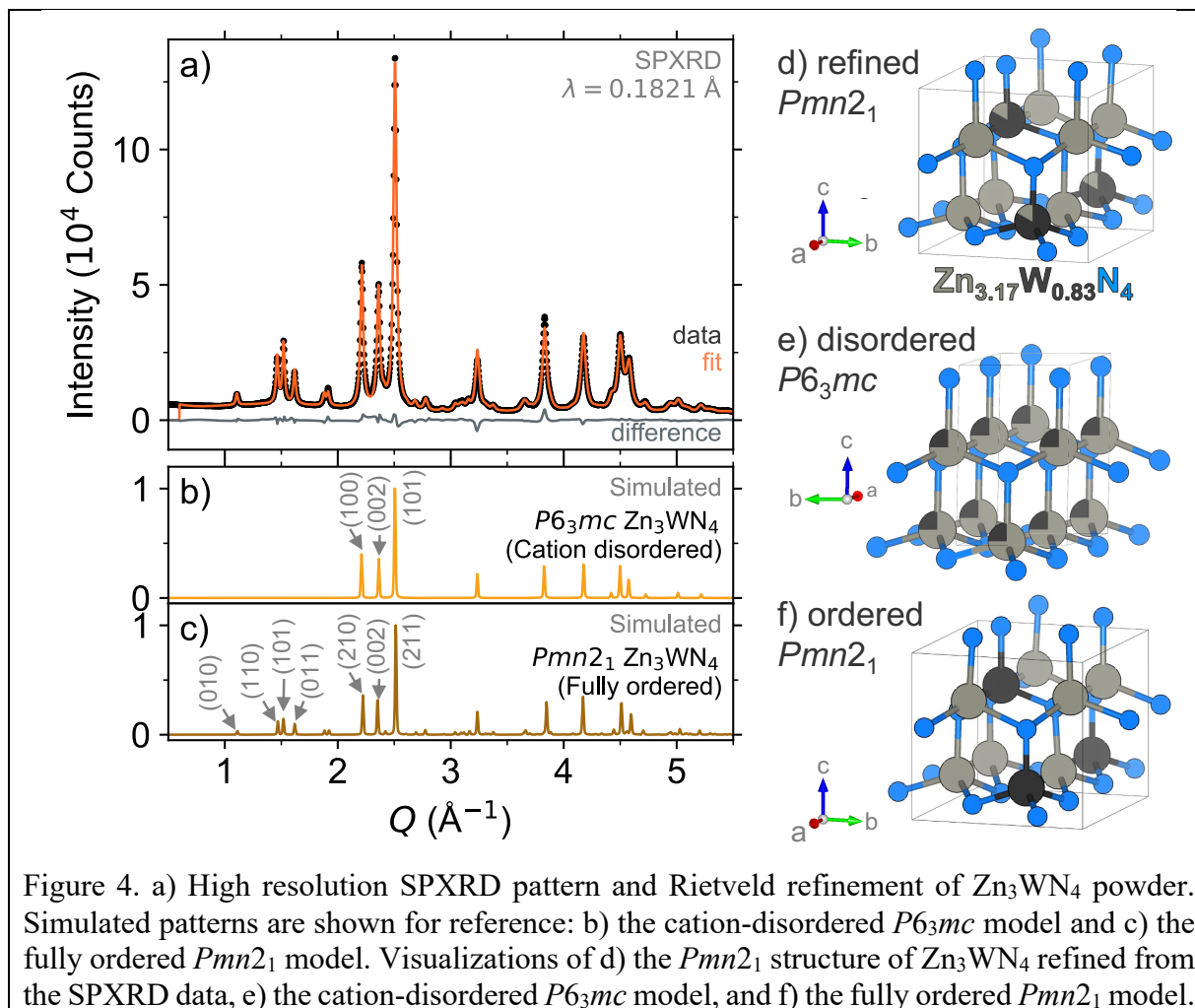
The lower exothermicity of the ZnBr_2 -based reaction leads to a more controlled release of heat and greater product purity, compared to the ZnCl_2 -based reaction. DSC measurements show that the ZnBr_2 reaction has three small exotherms (Figure 3a). A gradual exotherm starts near 190 °C (a-i), followed by two exotherms near 305 °C (a-ii) and 334 °C (a-iii). This third event may be preceded by a very minor endotherm, possibly consistent with Li_2ZnBr_4 melting. This reactivity occurs well below the 392 °C melting point of ZnBr_2 , suggesting the process is a solid-state reaction. The ZnCl_2 reaction (Figure 3b) starts similarly, with a gradual exotherm between 190 °C and 280 °C (b-i). Then at ≈ 280 °C, a massive exotherm (b-ii) initiates just below the melting point of ZnCl_2 (325 °C). This event likely corresponds to the formation of a liquid phase, such as a LiCl - ZnCl_2 eutectic (287 °C at 91% ZnCl_2).^[59] Peak b-ii has curvature because this event releases heat so quickly that the DSC stage increases in temperature by approximately 15 °C, after which the DSC pan cools slightly. This kind of rapid exothermic event is common in metathesis reactions; once a liquid phase forms, reaction kinetics accelerate and the heat release self-propagates.^[36] Lastly, a small endotherm is observed at 336 °C (b-iii), consistent with the melting of Li_2ZnCl_4 . These results are broadly consistent with the *in situ* SPXRD results, albeit shifted slightly in temperature owing to differences in experimental configuration.

These DSC results show why the ZnBr_2 reaction yields the purest product while the ZnCl_2 reactions exhibit a small Zn impurity. The rapid release of heat in the ZnCl_2 reaction may cause small portions of the material to decompose: $\text{Zn}_3\text{WN}_4 \rightarrow \text{W} + 3 \text{Zn} + 2 \text{N}_2$ or $\text{Zn}_3\text{WN}_4 \rightarrow \text{WN} + 3$

$\text{Zn} + 3/2 \text{N}_2$ (Figure S4). In contrast, the washed product of the ZnBr_2 synthesis yielded a PXRD pattern with all Bragg peaks indexed to $Pmn2_1$ Zn_3WN_4 . These differences can easily be seen in the color of the material (see insets, Figure 3), where Zn impurities in the ZnCl_2 reaction led to a grey color. The Zn_3WN_4 sample produced by the ZnBr_2 reaction is brown. These *in situ* SPXRD and DSC measurements guided our optimization of the synthesis for Zn_3WN_4 .

Structural and composition analysis of Zn_3WN_4

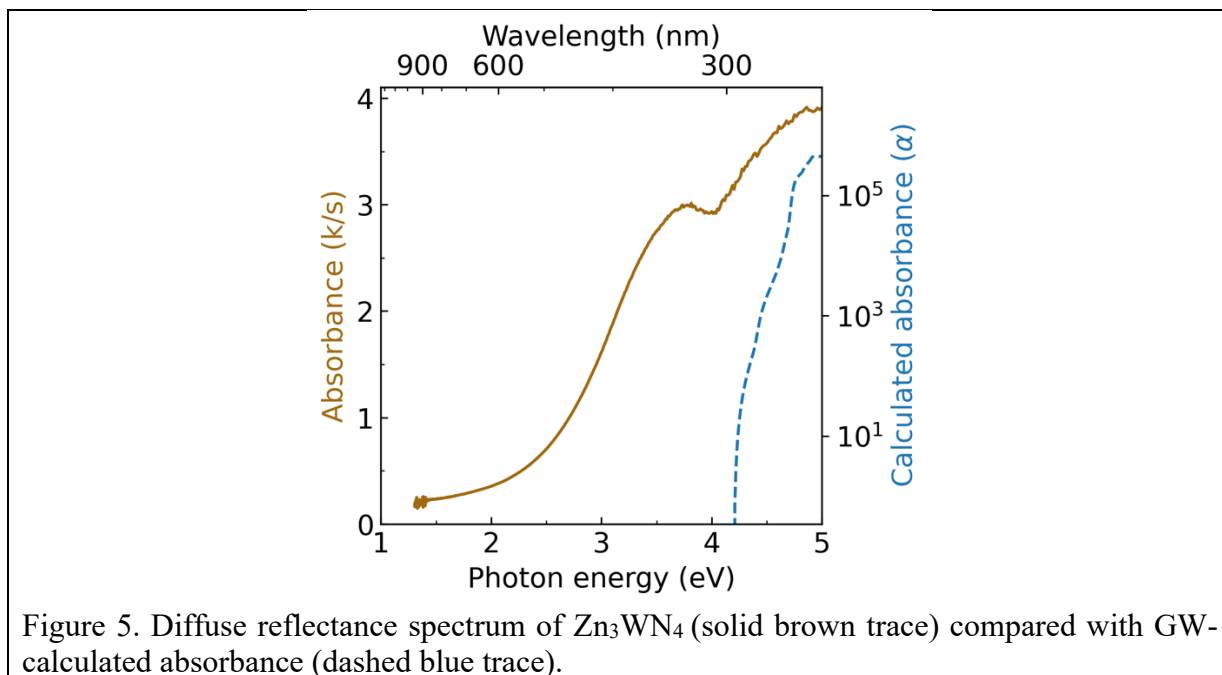
The best conditions we found were to heat ZnBr_2 with Li_6WN_4 at a ramp of $+5^\circ\text{C}/\text{min}$ to 300°C for a 1 h dwell, followed by natural cooling in the furnace. This reaction was scaled up to ca. 1 g reactant mix for *ex situ* analysis. Washing with anhydrous methanol successfully removed byproduct LiBr and excess ZnBr_2 while preserving the targeted phase. We used a slight excess of ZnBr_2 ($3.1 \text{ ZnBr}_2 + \text{Li}_6\text{WN}_4$) to ensure complete conversion and minimize reaction temperature by acting as a heat sink. XRF measurements show a Zn:W ratio of $3.165(3):1$, slightly higher than expected than the 3:1 ratio of Zn_3WN_4 (representative XRF spectrum shown in Figure S5), which may be a result of the excess ZnBr_2 . PXRD techniques confirmed that this synthesis of Zn_3WN_4 proceeded without the formation of decomposition products (i.e., Zn, $(\text{Zn},\text{W})\text{N}_x$ phases).



High resolution SPXRD measurements confirm the successful synthesis of Zn_3WN_4 (Figure 4). Rietveld analysis of the SPXRD data (Figure 4a) shows that Zn_3WN_4 crystallizes in space group $Pmn2_1$ with lattice parameters $a = 6.5602(8)$ Å, $b = 5.6813(7)$ Å, and $c = 5.3235(2)$ Å. The presence of intensity at the (010), (110), (101), and (101) Bragg positions indicates a substantial degree of cation ordering. The peaks for the (210), (002), and (211) reflections are characteristic of wurtzite-derived structures; these correspond to the (100), (002), and (101) reflections in the prototypical wurtzite structure ($P6_3mc$), respectively (Figure 4b). Rietveld-refined occupancies suggest a Zn:W ratio of 3.8:1, a higher ratio than that measured by XRF (3.2:1), with partial occupancy of Zn on the W site (Table S1), indicating a composition of $\text{Zn}_{3.17}\text{W}_{0.83}\text{N}_4$ (Figure 4d). The occupancy of the N atoms refined to 1 within error and so was fixed at unity. Alternative structural models were also considered (Table S2, Figures S6–S8), as discussed further in the section on cation ordering in Zn_3WN_4 .

Property measurements

Diffuse reflectance spectroscopy measurements reveal two absorption onsets for Zn_3WN_4 : one near 2.5 eV and another near 4.0 eV (Figure 5). This first feature is similar to the 2.0 eV to 2.4 eV absorption onset reported for cation disordered Zn_3MoN_4 and Zn_3WN_4 synthesized as thin films.^[29,60] The second absorption feature occurs near 4.0 eV, which is consistent with the expected bandgap for fully cation-ordered Zn_3WN_4 in the $Pmn2_1$ space group. The GW-calculated indirect band gap is 3.96 eV, with a direct bandgap of 4.20 eV (NREL MatDB ID 287103; blue trace in Figure 5).^[61,62] Other researchers using a hybrid functional, HSE06, calculated the bandgap to be 3.60 eV.^[27] These two features therefore suggest that our Zn_3WN_4 powder sample is a mixture of cation-ordered and cation-disordered structures. Magnetic susceptibility measurements are consistent with the presence of an impurity, as the material does not exhibit purely diamagnetic behavior (Figure S9).



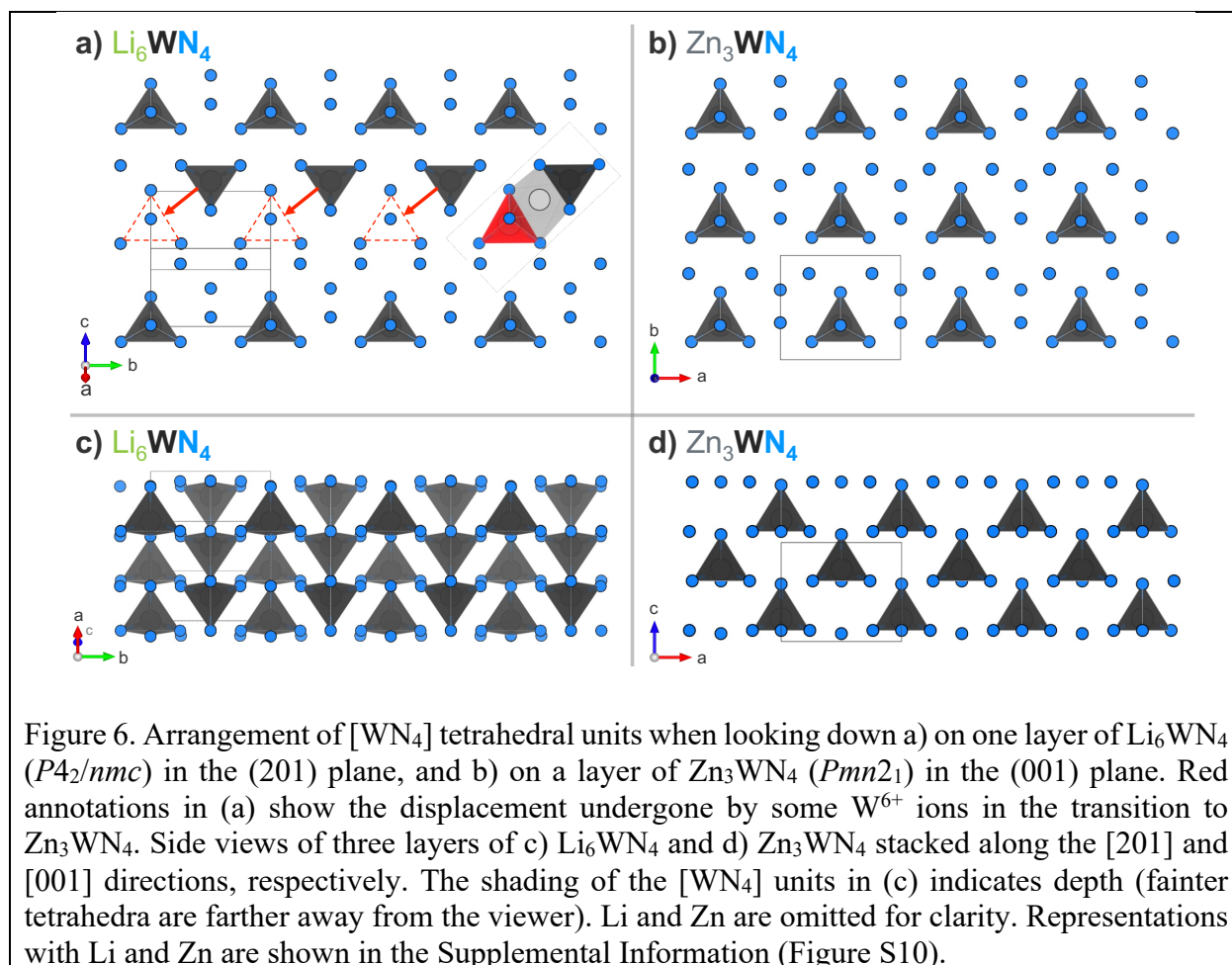
Cation ordering in Zn_3WN_4

Our metathesis approach yielded a different polytype for Zn_3WN_4 compared to prior thin film syntheses. We show here that metathesis between Li_6WN_4 and ZnBr_2 successfully synthesized Zn_3WN_4 in space group $Pmn2_1$ (Figure 4). In contrast, prior thin film sputtering work produced cation-disordered $P6_3mc$ structures.^[2,29,60] While both the $Pmn2_1$ and $P6_3mc$ structures are wurtzite-derived, the cation-ordered structure is expected to be the thermodynamic ground state.^[2,26] In thin film sputtering, high-energy plasma precursors deposit onto a substrate and quench rapidly in a local energy minimum, thus locking in the disordered cation arrangement.^[26] While bulk syntheses can sometimes lead to cation-disordered structures,^[6,10,45,46,49] the high charge on W (6+) likely encourages ordering to maximize the spacing between the hexavalent cations. The kinetics of our bulk metathesis reactions here proceed in a way that avoids the local energy minimum of the disordered structure, instead forming a (mostly) ordered structure.

The degree of cation ordering in our Zn_3WN_4 sample cannot be precisely determined from our current SPXRD data. While the SPXRD results suggest that Zn_3WN_4 was synthesized in a (mostly) cation ordered form (Figure 4), our optical spectroscopy results suggest that some degree of cation disorder may be present (Figure 5). Notably, the same batch of Zn_3WN_4 was used to create samples for the diffuse reflectance optical spectroscopy, magnetometry, XRF, and high resolution SPXRD measurements. The single-phase model includes some site disorder, leading to a refined composition of $\text{Zn}_{3.17}\text{W}_{0.83}\text{N}_4$ and a good statistical fit ($R_{\text{wp}} = 3.989\%$). Attempts to model the pattern with two phases (a cation-ordered $Pmn2_1$ and a cation-disordered $P6_3mc$) yield a similar fit quality as the single-phase fit (Figure S6). The two-phase refinements suggest the powder may be approximately 10–20 mol% $P6_3mc$. These two-phase models are consistent with our optical data, as disordered $P6_3mc$ Zn_3WN_4 likely exhibits lower-energy absorption (ca. 2.5 eV)^[29] compared to cation-ordered $Pmn2_1$ Zn_3WN_4 , which has a predicted bandgap of ca. 4.0 eV.^[27] However, the small difference in statistical fit for the best two-phase model ($R_{\text{wp}} = 3.742\%$) relative to the best single-phase model ($R_{\text{wp}} = 3.989\%$) suggests that determining the precise cation order of the material is non-trivial (see the Supplemental Information for more discussion). In sum, these results indicate that our batch of cation-ordered Zn_3WN_4 exhibits some degree of disorder or inhomogeneity on the order of 10–20 mol%. Although our Zn_3WN_4 sample is not perfectly ordered, it exhibits a substantially larger degree of cation ordering than prior thin film work.^[29,60]

Structural relation of precursor and product

The synthesis reported here is distinct from literature on prior ion exchange syntheses of nitrides in that the ions undergoing exchange have different formal charges. All prior reports on nitrides exchanged ions of the same charge (e.g., displacing Na^+ with Cu^+ in $A\text{Ta}\text{N}_2$, or Ca^{2+} with Mg^{2+} in $A_2\text{Si}_5\text{N}_8$; where A represents the exchangeable cations).^[47,50,51] Here, we replace a monovalent cation (Li^+) with a divalent cation (Zn^{2+}). While such exchange has been conducted in chalcogenides (e.g., $2 \text{NaCrS}_2 + \text{MgCl}_2 \rightarrow \text{MgCr}_2\text{S}_4 + 2 \text{NaCl}$),^[63] to the best of our knowledge this is the first report of such an exchange in nitrides. The resulting decrease in the cation:anion ratio (from 7:4 to 4:4) means that a truly topotactic replacement is unlikely to occur. However, the transformation appears to be near-topotactic.

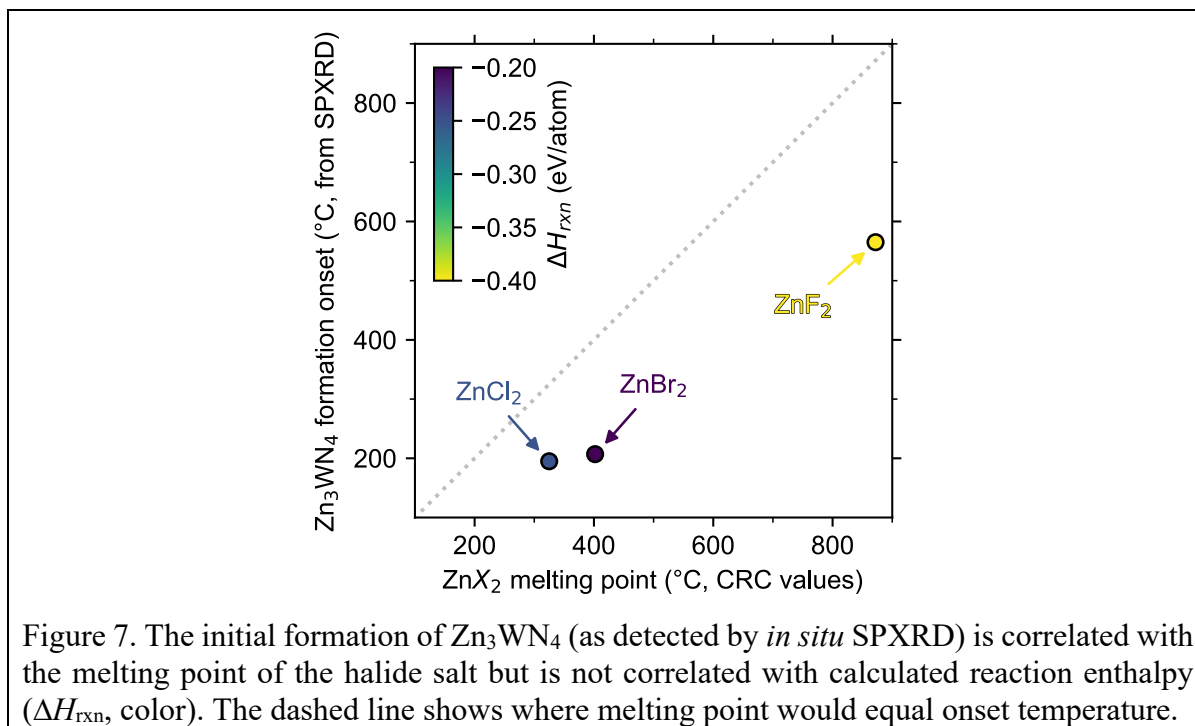


The transformation from Li_6WN_4 to Zn_3WN_4 involves slight structural rearrangements (Figure 6). The W^{6+} retains its tetrahedral coordination and (for the most part) its oxidation state through the process, but the orientation of the polyhedra changes. The fcc anion lattice of Li_6WN_4 converts to the hcp anion lattice of Zn_3WN_4 . During this change, half of the W^{6+} ions in Li_6WN_4 migrate through an octahedral site to a new tetrahedral site in Zn_3WN_4 (red annotations). The anion packing layers also decrease in spacing from 2.767(1) Å in Li_6WN_4 to 2.662(1) Å in Zn_3WN_4 . The shortest W–W distance decreases from 4.927(1) Å to 4.646(1) Å. Lastly, the centrosymmetric structure of Li_6WN_4 ($P4_2/nmcS$) converts to a polar structure of Zn_3WN_4 ($Pmn2_1$). We did not observe any signs of solid solution behavior (i.e., $\text{Li}_{6-x}\text{Zn}_{x/2}\text{WN}_4$) in the *in situ* SPXRD studies; however, solid solution behavior may be present but undetected by the *in situ* SPXRD data if it occurs on short timescales (<30 s) or small length scales (ca 10 nm).

Reaction pathway

Our results demonstrate that the halide anion X in ZnX_2 exerts a powerful influence over the metathesis reaction thermodynamics and kinetics of Zn-containing ternary nitrides. *In situ* SPXRD and DSC measurements reveal that the phase purity of the product is correlated with the melting points of the phases and the reaction energy (Figure 7). The ZnF_2 -based reaction is highly exothermic, and ZnF_2 has a high melting point. These two factors result in high-temperature reactivity and partial Zn_3WN_4 phase decomposition. In contrast, ZnCl_2 and ZnBr_2 react at much

lower temperatures (owing to the formation of liquid phases) and release less energy during the reaction. However, the slightly lower melting point of ZnCl_2 compared to ZnBr_2 combined with the slightly higher ΔH_{rxn} of the respective reaction leads to a runaway exothermic event (Figure 3) and slight Zn_3WN_4 decomposition. Overall, the ZnBr_2 -based reactions were optimal for the synthesis of Zn_3WN_4 because of the low ΔH_{rxn} and the low melting point of ZnBr_2 , but further optimization for phase purity may be needed in future research on other materials.



This type of reaction control has been explored in oxides but has not previously been detailed for ternary nitrides. “Spectator ions” that are not incorporated into the final product still have substantial influence over reaction pathways and polymorph formation, as demonstrated for syntheses of Y-Mn-O phases.^[64–69] In particular, work on “co-metathesis” identified that when eutectic halide mixtures form *in situ*, these liquids decrease reactant onset temperatures relative to systems without eutectics.^[68,69] Similar eutectics are likely forming between ZnX_2 and LiX in our syntheses of Zn_3WN_4 .

Generalizability to other materials

There are numerous Zn-M-N phases that have been demonstrated to be synthesizable via thin film sputtering but that have not yet been made in bulk. In addition to main-group-containing compounds (e.g., ZnGeN_2 , ZnSnN_2),^[70,71] sputtering has been used to synthesize fully nitridized transition metal ternaries: ZnTiN_2 , ZnZrN_2 , Zn_2VN_3 , Zn_2NbN_3 , Zn_2TaN_3 , Zn_3MoN_4 , and Zn_3WN_4 .^[2,3,25,26,29] Although computational predictions for these thin film materials find that cation-ordered structures are the thermodynamic ground state (Figure 4f),^[72] these sputtered films tend to form in cation-disordered structure variants (Figure 4e).^[2,3] This disorder tends to decrease the bandgap of the material by creating localized electronic states.^[7,73] Bulk syntheses of these materials could advance the development of these new semiconductors by studying the effect of structure (e.g., ordering) on optoelectronic properties of these new semiconductors.

The synthesis of Zn_3WN_4 from Li_6WN_4 and ZnX_2 suggests a promising strategy for future materials discovery of cation-ordered heterovalent ternary nitrides via metathesis from lithium-based ternary nitride precursors. Lithium-based ternary nitrides are the most well-studied subset of ternary nitrides,^[2] suggesting that many Li-*M*-N phases exist that could be used to synthesize additional *A*-*M*-N phases via exchange with AX_n (where *A* and *M* are metals and *X* is a halide). Following our results here, *X* should be selected to minimize reaction energy and thus minimize the risk of decomposing the target phase via gaseous N_2 loss. To demonstrate this point, we also synthesized Zn_3MoN_4 from Li_6MoN_4 and ZnBr_2 (Figure S11). Zn_3MoN_4 was the main product, but some decomposition products were also observed, indicating that additional reaction optimization is needed. Unlike in Zn_3WN_4 , the ZnBr_2 -based reaction was not sufficiently low-energy to avoid this decomposition for Zn_3MoN_4 (Figure S11). While we were not able to synthesize phase-pure Zn_3MoN_4 here, further reaction engineering, like adding NH_4Cl to manage heat flow,^[40,41,43,44] may be able to produce phase-pure Zn_3MoN_4 . As we found that the reaction onset temperature is correlated with AX_2 melting point, phases with high-melting temperature precursors may be difficult to synthesize below the decomposition point of the targeted ternary. Therefore, future work should consider ways to decouple the reaction onset from the AX_2 melting point. In sum, this work shows how Li-*B*-N phases can be promising precursors for accelerating the discovery of new ternary nitrides.

Conclusions

Here, we report the bulk synthesis of cation-ordered Zn_3WN_4 , through ion exchange reactions beginning from Li-based ternary nitride precursors: $\text{Li}_6\text{WN}_4 + \text{ZnX}_2 \rightarrow \text{Zn}_3\text{WN}_4 + 6 \text{LiX}$ (*X* = F, Cl, Br). These reactions proceed directly (i.e., without intermediates), as measured by *in situ* synchrotron powder X-ray diffraction and differential scanning calorimetry. The reaction onset temperature correlates with the melting point of the ZnX_2 precursor, allowing ZnCl_2 - and ZnBr_2 -based reactions to proceed at ≤ 300 °C. The more exothermic reactions led to greater degree of Zn_3WN_4 decomposition, meaning that the least exothermic reaction (with ZnBr_2) is the most favorable for synthesis. High resolution synchrotron powder X-ray diffraction data is consistent with cation-ordered Zn_3WN_4 (*Pmn*2₁). This finding is distinct from prior thin film syntheses, which yielded cation-disordered *P*6₃*mc* Zn_3WN_4 . Diffuse reflectance spectroscopy shows that Zn_3WN_4 powders exhibit absorption onsets near 2.5 eV and 4.0 eV, suggesting that a small amount of a cation-disordered *P*6₃*mc* phase of Zn_3WN_4 may be mixed in with the cation-ordered *Pmn*2₁ phase. Preliminary work targeting Zn_3MoN_4 from Li_6MoN_4 and ZnBr_2 suggests this synthesis approach may readily extend to other systems. These findings indicate that Li-*M*-N compounds may serve as precursors for synthesizing numerous other ternary nitrides.

Acknowledgements

This work was authored at the National Renewable Energy Laboratory, operated by Alliance for Sustainable Energy, LLC, for the U.S. Department of Energy (DOE) under Contract No. DE-AC36-08GO28308. Funding provided by DOE Basic Energy Sciences Early Career Award “Kinetic Synthesis of Metastable Nitrides.” This research used resources of the Advanced Photon Source, a U.S. Department of Energy (DOE) Office of Science user facility operated for the DOE Office of Science by Argonne National Laboratory under Contract No. DE-AC02-06CH11357. R.A.K. (SPXRD measurements) gratefully acknowledges support from the U.S. DOE Office of Energy Efficiency and Renewable Energy (EERE), Hydrogen and Fuel Cell Technologies Office (HFTO). R.W.S. acknowledges support from the Director’s Fellowship within NREL’s Laboratory Directed Research and Development program, and K.H. acknowledges support from the DOE Science Undergraduate Laboratory Internships (SULI) program. The authors thank Dr. Robert Bell and Dr. Noemi Leick for technical support with DSC measurements, Dr. Fred Baddour for support with the laboratory PXRD measurements, Dr. Wenqian Xu for support with the *in situ* SPXRD measurements, and Dr. Stephan Lany for calculating the absorption coefficient of $Pmn2_1$ Zn_3WN_4 . The views expressed in the article do not necessarily represent the views of the DOE or the U.S. Government.

Author Contributions

Christopher L. Rom: Conceptualization, Investigation, Formal analysis, Visualization, Writing-Original draft preparation

Shaun O’Donnell: Investigation

Kayla Huang: Investigation

Ryan A. Klein: Investigation, Formal analysis

Morgan J. Kramer: Investigation, Formal analysis

Rebecca W. Smaha: Investigation

Andriy Zakutayev: Conceptualization, Funding acquisition, Supervision, Writing-Reviewing and Editing

References

- [1] A. L. Greenaway, C. L. Melamed, M. B. Tellekamp, R. Woods-Robinson, E. S. Toberer, J. R. Neilson, A. C. Tamboli, *Annu. Rev. Mater. Res.* **2021**, *51*, 591–618.
- [2] W. Sun, C. J. Bartel, E. Arca, S. R. Bauers, B. Matthews, B. Orvañanos, B.-R. Chen, M. F. Toney, L. T. Schelhas, W. Tumas, J. Tate, A. Zakutayev, S. Lany, A. M. Holder, G. Ceder, *Nat. Mater.* **2019**, *18*, 732–739.
- [3] A. Zakutayev, S. R. Bauers, S. Lany, *Chem. Mater.* **2022**, *34*, 1418–1438.
- [4] A. Zakutayev, *J. Mater. Chem. A* **2016**, *4*, 6742–6754.
- [5] W. Sun, S. T. Dacek, S. P. Ong, G. Hautier, A. Jain, W. D. Richards, A. C. Gamst, K. A. Persson, G. Ceder, *Sci. Adv.* **2016**, *2*, e1600225.
- [6] E. W. Blanton, K. He, J. Shan, K. Kash, *J. Cryst. Growth* **2017**, *461*, 38–45.
- [7] R. R. Schnepf, J. J. Cordell, M. B. Tellekamp, C. L. Melamed, A. L. Greenaway, A. Mis, G. L. Brennecka, S. Christensen, G. J. Tucker, E. S. Toberer, S. Lany, A. C. Tamboli, *ACS Energy Lett.* **2020**, *5*, 2027–2041.
- [8] I. S. Khan, K. N. Heinselman, A. Zakutayev, *J. Phys. Energy* **2020**, *2*, 032007.

- [9] A. D. Martinez, A. N. Fioretti, E. S. Toberer, A. C. Tamboli, *J. Mater. Chem. A* **2017**, *5*, 11418–11435.
- [10] F. Kawamura, N. Yamada, M. Imai, T. Taniguchi, *Cryst. Res. Technol.* **2016**, *51*, 220–224.
- [11] J. Häusler, S. Schimmel, P. Wellmann, W. Schnick, *Chem. – Eur. J.* **2017**, *23*, 12275–12282.
- [12] R. Juza, F. Hund, *Naturwissenschaften* **1946**, *33*, 121–122.
- [13] M. Y. Chern, F. J. DiSalvo, *J. Solid State Chem.* **1990**, *88*, 528–533.
- [14] H. Yamane, F. J. DiSalvo, *J. Solid State Chem.* **1995**, *119*, 375–379.
- [15] W. L. Larson, H. P. Maruska, D. A. Stevenson, *J. Electrochem. Soc.* **1974**, *121*, 1673.
- [16] Q.-H. Zhang, J. Wang, C.-W. Yeh, W.-C. Ke, R.-S. Liu, J.-K. Tang, M.-B. Xie, H.-B. Liang, Q. Su, *Acta Mater.* **2010**, *58*, 6728–6735.
- [17] M. Wintenberger, M. Maunaye, Y. Laurent, *Mater. Res. Bull.* **1973**, *8*, 1049–1053.
- [18] O. E. O. Zeman, F. O. von Rohr, L. Neudert, W. Schnick, *Z. Für Anorg. Allg. Chem.* **2020**, *646*, 228–233.
- [19] Y. Sun, Y. Guo, Y. Tsujimoto, J. Yang, B. Shen, W. Yi, Y. Matsushita, C. Wang, X. Wang, J. Li, C. I. Sathish, K. Yamaura, *Inorg. Chem.* **2013**, *52*, 800–806.
- [20] S. Deng, Y. Sun, H. Wu, Z. Shi, L. Wang, J. Yan, K. Shi, P. Hu, X. Diao, Q. Huang, C. Sürgers, C. Wang, *Scr. Mater.* **2018**, *146*, 18–21.
- [21] M. Li, J. Lu, K. Luo, Y. Li, K. Chang, K. Chen, J. Zhou, J. Rosen, L. Hultman, P. Eklund, P. O. Å. Persson, S. Du, Z. Chai, Z. Huang, Q. Huang, *J. Am. Chem. Soc.* **2019**, *141*, 4730–4737.
- [22] O. Beckmann, H. Boller, H. Nowotny, F. Benesovsky, *Monatshefte Für Chem. Chem. Mon.* **1969**, *100*, 1465–1470.
- [23] W. Jeitschko, H. Nowotny, F. Benesovsky, *Monatshefte Für Chem. Verwandte Teile Anderer Wiss.* **1964**, *95*, 1212–1218.
- [24] W. Wang, X. Kan, X. Liu, Z. Cheng, C. Liu, M. Shezad, Y. Yang, Q. Lv, K. Mehmood Ur Rehman, *Eur. Phys. J. Plus* **2020**, *135*, 505.
- [25] A. L. Greenaway, S. Ke, T. Culman, K. R. Talley, J. S. Mangum, K. N. Heinselman, R. S. Kingsbury, R. W. Smaha, M. K. Gish, E. M. Miller, K. A. Persson, J. M. Gregoire, S. R. Bauers, J. B. Neaton, A. C. Tamboli, A. Zakutayev, *J. Am. Chem. Soc.* **2022**, *144*, 13673–13687.
- [26] R. Woods-Robinson, V. Stevanović, S. Lany, K. N. Heinselman, M. K. Horton, K. A. Persson, A. Zakutayev, *Phys. Rev. Mater.* **2022**, *6*, 043804.
- [27] D. Chu, Y. Huang, C. Xie, E. Tikhonov, I. Kruglov, G. Li, S. Pan, Z. Yang, *Angew. Chem.* **2023**, *135*, e202300581.
- [28] G. Paniconi, Z. Stoeva, R. I. Smith, P. C. Dippo, B. L. Gallagher, D. H. Gregory, *J. Solid State Chem.* **2008**, *181*, 158–165.
- [29] E. Arca, S. Lany, J. D. Perkins, C. Bartel, J. Mangum, W. Sun, A. Holder, G. Ceder, B. Gorman, G. Teeter, W. Tumas, A. Zakutayev, *J. Am. Chem. Soc.* **2018**, *140*, 4293–4301.
- [30] E. Horvath-Bordon, R. Riedel, A. Zerr, P. F. McMillan, G. Auffermann, Y. Prots, W. Bronger, R. Kniep, P. Kroll, *Chem. Soc. Rev.* **2006**, *35*, 987–1014.
- [31] A. J. Martinolich, J. A. Kurzman, J. R. Neilson, *J. Am. Chem. Soc.* **2016**, *138*, 11031–11037.
- [32] R. B. Kaner, C. H. Wallace, *Process for Rapid Solid-State Formation of Refractory Nitrides*, **2000**, US6120748A.

- [33] R. B. Kaner, P. R. Bonneau, E. G. Gillan, J. B. Wiley, R. F. J. Jr, R. Treece, *Rapid Solid-State Synthesis of Refractory Materials*, **1992**, US5110768A.
- [34] E. G. Gillan, R. B. Kaner, *Inorg. Chem.* **1994**, *33*, 5693–5700.
- [35] L. Rao, R. B. Kaner, *Inorg. Chem.* **1994**, *33*, 3210–3211.
- [36] E. G. Gillan, R. B. Kaner, *Chem. Mater.* **1996**, *8*, 333–343.
- [37] C. H. Wallace, T. K. Reynolds, R. B. Kaner, *Chem. Mater.* **1999**, *11*, 2299–2301.
- [38] J. L. O’Loughlin, C. H. Wallace, M. S. Knox, R. B. Kaner, *Inorg. Chem.* **2001**, *40*, 2240–2245.
- [39] J. B. Wiley, R. B. Kaner, *Science* **1992**, *255*, 1093–1097.
- [40] R. A. Janes, M. Aldissi, R. B. Kaner, *Chem. Mater.* **2003**, *15*, 4431–4435.
- [41] R. A. Janes, M. A. Low, R. B. Kaner, *Inorg. Chem.* **2003**, *42*, 2714–2719.
- [42] C. H. Wallace, S.-H. Kim, G. A. Rose, L. Rao, J. R. Heath, M. Nicol, R. B. Kaner, *Appl. Phys. Lett.* **1998**, *72*, 596–598.
- [43] A. J. Anderson, R. G. Blair, S. M. Hick, R. B. Kaner, *J. Mater. Chem.* **2006**, *16*, 1318–1322.
- [44] R. W. Cumberland, R. G. Blair, C. H. Wallace, T. K. Reynolds, R. B. Kaner, *J. Phys. Chem. B* **2001**, *105*, 11922–11927.
- [45] C. L. Rom, M. J. Fallon, A. Wustrow, A. L. Prieto, J. R. Neilson, *Chem. Mater.* **2021**, *33*, 5345–5354.
- [46] P. K. Todd, M. J. Fallon, J. R. Neilson, A. Zakutayev, *ACS Mater. Lett.* **2021**, *3*, 1677–1683.
- [47] P. Bielec, W. Schnick, *Angew. Chem. Int. Ed.* **2017**, *56*, 4810–4813.
- [48] P. Bielec, O. Janka, T. Block, R. Pöttgen, W. Schnick, *Angew. Chem. Int. Ed.* **2018**, *57*, 2409–2412.
- [49] C. L. Rom, A. Novick, M. J. McDermott, J. R. Gallawa, G. T. Tran, D. C. Asebiah, B. C. McBride, R. C. Miller, A. L. Prieto, E. Toberer, V. Stevanovic, A. Zakutayev, **n.d.**
- [50] U. Zachwieja, H. Jacobs, *Eur. J. Solid State Inorg. Chem.* **1991**, *28*, 1055–1062.
- [51] M. Yang, A. Zakutayev, J. Vidal, X. Zhang, D. S. Ginley, F. J. DiSalvo, *Energy Environ. Sci.* **2013**, *6*, 2994–2999.
- [52] A. Miura, M. Lowe, B. M. Leonard, C. V. Subban, Y. Masubuchi, S. Kikkawa, R. Dronskowski, R. G. Hennig, H. D. Abruña, F. J. DiSalvo, *J. Solid State Chem.* **2011**, *184*, 7–11.
- [53] A. Stein, S. W. Keller, T. E. Mallouk, *Science* **1993**, *259*, 1558–1564.
- [54] *Z. Für Krist. - Cryst. Mater.* **1984**, *166*, 189–197.
- [55] W. X. Yuan, J. W. Hu, Y. T. Song, W. J. Wang, Y. P. Xu, *Powder Diffr.* **2005**, *20*, 18–21.
- [56] A. Pfitzner, J. K. Crockcroft, I. Solinas, H. D. Lutz, *Z. Für Anorg. Allg. Chem.* **1993**, *619*, 993–998.
- [57] J. N. Law, S. Pandey, P. Gorai, P. C. St. John, *JACS Au* **2023**, *3*, 113–123.
- [58] C. Martin, A. Durif-Varambon, J.-C. Joubert, *Bull. Minéralogie* **1965**, *88*, 141–141.
- [59] S. J. Shaw, G. S. Perry, *Thermochim. Acta* **1989**, *155*, 87–96.
- [60] B. E. Matthews, “Synthesis and Analysis of Heterostructural Semiconductor Alloy $\text{Sn}_{1-x}\text{Ca}_x\text{Ch}$ ($\text{Ch}=\text{S}, \text{Se}$) and Nitrides $\text{Zn}_{1-x}\text{W}_x\text{N}$ and $\text{Zn}_{1-x}(\text{W}_{1-y}\text{Mo}_y)_x\text{N}$,” Dissertation **2018**
- [61] S. Lany, *J. Phys. Condens. Matter* **2015**, *27*, 283203.
- [62] S. Lany, *Phys. Rev. B* **2013**, *87*, 085112.
- [63] A. Miura, H. Ito, C. J. Bartel, W. Sun, N. Carolina Rosero-Navarro, K. Tadanaga, H. Nakata, K. Maeda, G. Ceder, *Mater. Horiz.* **2020**, *7*, 1310–1316.

- [64] J. R. Neilson, M. J. McDermott, K. A. Persson, *J. Mater. Res.* **2023**, 38, 2885–2893.
- [65] P. K. Todd, A. M. M. Smith, J. R. Neilson, *Inorg. Chem.* **2019**, 58, 15166–15174.
- [66] P. K. Todd, J. R. Neilson, *J. Am. Chem. Soc.* **2019**, 141, 1191–1195.
- [67] P. K. Todd, M. J. McDermott, C. L. Rom, A. A. Corrao, J. J. Denney, S. S. Dwaraknath, P. G. Khalifah, K. A. Persson, J. R. Neilson, *J. Am. Chem. Soc.* **2021**, 143, 15185–15194.
- [68] A. Wustrow, M. J. McDermott, D. O’Nolan, C.-H. Liu, G. T. Tran, B. C. McBride, S. M. Vornholt, C. Feng, S. S. Dwaraknath, K. W. Chapman, S. J. L. Billinge, W. Sun, K. A. Persson, J. R. Neilson, *Chem. Mater.* **2022**, 34, 4694–4702.
- [69] A. Wustrow, G. Huang, M. J. McDermott, D. O’Nolan, C.-H. Liu, G. T. Tran, B. C. McBride, S. S. Dwaraknath, K. W. Chapman, S. J. L. Billinge, K. A. Persson, K. Thornton, J. R. Neilson, *Chem. Mater.* **2021**, 33, 3692–3701.
- [70] S. Kikkawa, H. Morisaka, *Solid State Commun.* **1999**, 112, 513–515.
- [71] F. Deng, H. Cao, L. Liang, J. Li, J. Gao, H. Zhang, R. Qin, C. Liu, *Opt. Lett.* **2015**, 40, 1282–1285.
- [72] W. Sun, A. Holder, B. Orvañanos, E. Arca, A. Zakutayev, S. Lany, G. Ceder, *Chem. Mater.* **2017**, 29, 6936–6946.
- [73] J. J. Cordell, G. J. Tucker, A. Tamboli, S. Lany, *APL Mater.* **2022**, 10, 011112.

Supplemental Information for: Bulk synthesis of Zn_3WN_4 via solid-state metathesis

Christopher L. Rom¹, Shaun O'Donnell^{1,2}, Kayla Huang^{1,3}, Ryan A. Klein^{1,4}, Morgan J. Kramer^{4,5}, Rebecca W. Smaha¹, Andriy Zakutayev^{1,*}

¹ Materials, Chemical, and Computational Science, National Renewable Energy Laboratory, Golden, CO, 80401, USA

² Department of Chemistry, Colorado State University, Fort Collins, CO, 80523, USA

³ University of Illinois Urbana-Champaign, Champaign, IL, 61801, USA

⁴ Center for Neutron Research, National Institute of Standards and Technology, Gaithersburg, MD, 20899, USA

⁵ Department of Chemistry, Southern Methodist University, Dallas, TX, 75275 USA

* Corresponding author: andriy.zakutayev@nrel.gov

Table of Contents

<i>Experimental</i>	18
Synthesis of Zn_3WN_4	18
Synthesis of Zn_3MoN_4	18
<i>In situ</i> synchrotron powder X-ray diffraction analysis.....	19
<i>Ex situ</i> powder X-ray diffraction analysis.....	19
Compositional, thermodynamic, and property measurements.....	20
<i>Additional PXRD measurements</i>	21
<i>In situ</i> variable temperature SPXRD measurements.....	22
Evidence of decomposition in the $3 \text{ZnCl}_2 + \text{Li}_6\text{WN}_4$ reaction.....	25
Compositional characterization.....	26
Structural models for the high resolution SPXRD measurements.....	27
Magnetic susceptibility measurements.....	32
Full structure visualizations of Li_6WN_4 and Zn_3WN_4	33
Synthesis of Zn_3MoN_4	33
<i>References</i>	35

Experimental

Synthesis of Zn_3WN_4

As some precursors are highly moisture sensitive, all precursors were prepared and stored in an argon-filled glovebox ($\text{O}_2 < 0.1$ ppm, $\text{H}_2\text{O} < 0.1$ ppm) unless explicitly mentioned. ZnF_2 ($\geq 99\%$, anhydrous, Alfa Aesar), ZnCl_2 ($\geq 99.995\%$, anhydrous, Sigma Aldrich), ZnBr_2 (99.999%, anhydrous, Aldrich), Li_3N ($\geq 99.5\%$, 80 mesh, Sigma Aldrich), W (99.95%, < 1 micron powder, Thermofisher Scientific) were used as received.

Li_6WN_4 was synthesized in a method modified from that of Yuan et al.^[1] Solid precursors (2.1 Li_3N + W, ca. 5 mol% excess Li_3N to account for loss by evaporation) were ground with a mortar and pestle and loaded into Zr crucibles with Zr lids (ca. 1 g loose powder). The Zr crucibles were then loaded into sacrificial quartz tubes (open on one end), which were loaded into quartz process tubes and heated in a tube furnace. Custom endcaps with quick disconnects enabled air-free transfer from the glovebox to the tube furnace (under Ar or N_2). The samples were reacted under flowing N_2 (50 sccm, 99.999% purity) with a $+5^\circ\text{C}/\text{min}$ ramp followed by a 12 h dwell at 850°C and then natural cooling after turning off the furnace. Samples were recovered into the glovebox for subsequent analysis and use. The beige-colored products were confirmed to be phase pure by powder X-ray diffraction (Figure S1).

Syntheses for Zn_3WN_4 were conducted by grinding together Li_6WN_4 with ZnX_2 ($X = \text{Cl}, \text{Br}$) in a ratio of approximately 1:3. The powders were pelletized with 6 mm diameter dies in an arbor press (ca. 100 mg per pellet), loaded into quartz ampules (10 mm OD, 10 mm ID, ca 10 cm length), sealed under vacuum (< 0.03 Torr), and heated in a muffle furnace. The optimized synthesis for Zn_3WN_4 used a ratio of $\text{Li}_6\text{WN}_4 + 3.1 \text{ ZnBr}_2$ and was scaled up to a 3 g batch, sealed in a quartz ampule under vacuum (< 0.03 Torr) and heated at $+5^\circ\text{C}/\text{min}$ to 300°C for a 1 h dwell, then allowed to cool naturally. Samples were recovered into the glovebox. Reaction byproduct LiX was washed away using anhydrous and degassed methanol that was dried over molecular sieves. For washing, centrifuge tubes were loaded with approximately 500 mg of product powder and 1.5 mL methanol. The tube was agitated with a vortex, centrifuged, and the supernatant was decanted. This wash was repeated for a total of 3 cycles. Recovered powders were dried overnight under vacuum. However, Zn_3WN_4 ultimately proved to be stable against air and water, and we note that the anhydrous washing may not be necessary.

Synthesis of Zn_3MoN_4

Just like Li_6WN_4 , Li_6MoN_4 was synthesized using Li_3N and Mo ($\geq 99.9\%$, 1–5 micron powder, Sigma Aldrich), following a method modified from that of Yuan et al.^[1] Heating the powders at 850°C for 12 h (with slight Li_3N excess) resulted in a phase pure Li_6MoN_4 (Figure S1b). This Li_6MoN_4 was then mixed with ZnBr_2 , pelletized, sealed in an ampule under vacuum, and heated at $+5^\circ\text{C}/\text{min}$ to 300°C for a 1 h dwell, followed by natural cooling. The product was then washed with anhydrous methanol.

In situ synchrotron powder X-ray diffraction analysis

In situ synchrotron powder X-ray diffraction (SPXRD) measurements were conducted at beamline 17-BM-B of the Advanced Photon Source at Argonne National Laboratory. For these experiments ($\lambda = 0.24101 \text{ \AA}$), the PerkinElmer plate detector was positioned 700 mm away from the sample. Homogenized precursors were packed into quartz capillaries in an Ar glovebox and flame-sealed under vacuum ($<30 \text{ mTorr}$). Capillaries were loaded into a flow-cell apparatus^[3] and heated at $5 \text{ }^\circ\text{C/min}$ to the specified temperature. A thermocouple was placed against the tip of the sample capillary, approximately 2 mm horizontally from the position of the X-ray beam. Diffraction pattern images were collected every 30 s by summing 20 exposures of 0.5 s each (10 s of summed exposure), followed by 20 s of deadtime. Images collected from the plate detector were radially integrated using GSAS-II and calibrated using a silicon standard.

Sequential Rietveld refinements were conducted on *in situ* SXPRD datasets using TOPAS Professional v6.^[4] Lattice parameters, background terms, and scale factors were refined for each phase as a function of temperature, while atomic coordinates and occupancies were held constant at the initial values of the reference structure. A weighted scale factor (W.S.F.) Q was calculated for each phase p as a product of scale factor S , cell volume V , and cell mass M : $Q_p = S_p \cdot V_p \cdot W_p$.^[5] We note that amorphous and liquid phases are inherently not observed in powder diffraction measurements and therefore cannot be accurately included in this analysis. A Lorentzian size broadening term was refined for each phase to model the peak shape using the pattern showing the greatest intensity of the relevant phase; this term was then fixed for the sequential refinements to better account for changes in intensity. To help stabilize the sequential refinement, isotropic displacement parameters (B_{iso}) were fixed at 1 \AA^2 for all atoms, but we note that this is likely not physical for a variable temperature investigation.

Ex situ powder X-ray diffraction analysis of Zn_3WN_4

The products of all reactions were characterized by powder X-ray diffraction (PXRD). Laboratory X-ray diffraction patterns were collected on a Rigaku Ultima IV diffractometer with $\text{Cu K}\alpha$ X-ray radiation at room temperature. All samples were initially prepared for PXRD measurements inside the glovebox; powder was placed on off-axis cut silicon single crystal wafers to reduce background scattering and then covered with polyimide tape to impede exposure to atmosphere. After Zn_3WN_4 was determined to be moderately air stable, PXRD patterns were collected without polyimide tape to decrease the background signal.

High resolution synchrotron powder X-ray diffraction (SPXRD) measurements were conducted at beamline 28-ID-2 of the National Synchrotron Light Source II ($\lambda = 0.1821 \text{ \AA}$) at Brookhaven National Laboratory. Samples were sealed under vacuum in quartz capillaries, which were then nested in Kapton capillaries. Data were collected for 60 seconds at $T = 25 \text{ }^\circ\text{C}$ while spinning. Scattered photon intensity was measured using a Perkin-Elmer XRD 1621 Digital Imaging Detector. The data were reduced using Dioptas.^[6] Pawley fits and subsequent Rietveld refinements were conducted using TOPAS Academic.^[4]

Rietveld refinements were conducted for the laboratory PXRD and SPXRD patterns using TOPAS and TOPAS Academic, v6 (Bruker AXS).^[4] Reference structures were sourced from the Inorganic

Crystal Structure Database (ICSD). The $Pmn2_1$ Zn_3MoN_4 structure (ICSD Col. Code 255744) was used as a starting model for $Pmn2_1$ Zn_3WN_4 , with the Mo replaced by W.^[7] For the cation disordered $P6_3mc$ Zn_3WN_4 structure, $P6_3mc$ ZnO was used as a starting model, with atomic occupancies adjusted to match the stoichiometry of Zn_3WN_4 , and lattice parameters adjusted to match the SPXRD pattern. For each structure, lattice parameters, isotropic displacement parameters, and general atomic coordinates were refined. For some models, Zn and W occupancy were refined as detailed in the Discussion section and the Supplemental (Figure S7). Structural visualizations and reference PXRD patterns were generated using VESTA.^[8]

Compositional, thermodynamic, and property measurements

The composition of nominal Zn_3WN_4 was measured by X-ray Fluorescence spectroscopy (XRF) and combustion analysis. Cation composition was quantified by XRF using a Bruker M4 Tornado with a Rh X-ray source. Samples were pelletized and XRF spectra were collected at 4 points across the pellet. Zn and W ratios were quantified from each spectra using the Bruker M4 software.

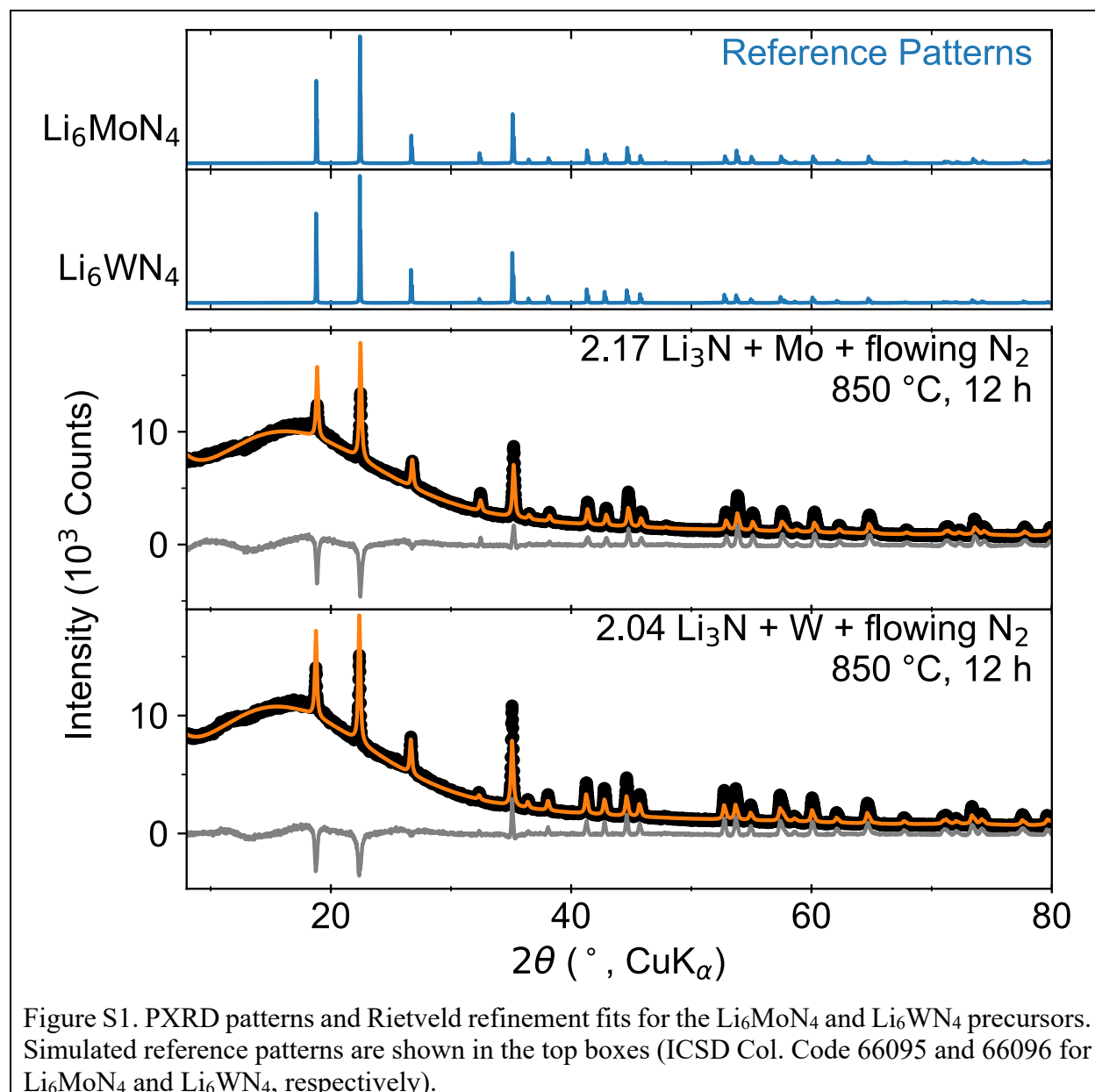
Differential scanning calorimetry (DSC) experiments were conducted using a Q20 system from TA Instruments. Samples were prepared in an Ar-filled glovebox. Samples (ca. 10 mg) were loaded into aluminum pans, which were crimped closed with an aluminum lid. The reference pan was also crimped closed under argon. Pans were then transferred out of the glovebox for measurement, and data were collected upon ramping up to 400 °C at a rate of 10 °C/min. Thermodynamic calculations for reaction enthalpies (ΔH_{rxn}) were conducted using formation enthalpy (ΔH_f) values reported in the Materials Project database.^[9,10]

UV-vis measurements were conducted on a Cary 6000 UV-Vis-NIR spectrometer. PTFE was used as a white reflectance standard. Absorbance was calculated with the Kubelka-Munk transformation, $k/s = (1 - R)^2 / 2R$ (where R is the reflectance, k is the apparent absorption coefficient, and s is the apparent scattering coefficient).

DC susceptibility data were measured on a Quantum Design Physical Properties Measurement System (PPMS) from $T = 2$ to 305 K in applied fields up to $\mu_0 H = 14$ T.

Additional PXRD measurements

Laboratory PXRD confirms the phase purity of the precursors that were synthesized for our metathesis reactions (Figure S1). All peaks index to the reference structures from the ICSD. The broad background at $2\theta < 35^\circ$ comes from the polyimide tape used to protect the powder from air and moisture. This background suppresses the measured peak intensities for peaks at $2\theta < 35^\circ$, leading to the poor fit for that region of the pattern.



In situ variable temperature SPXRD measurements

Figures S2 and S3 show the *in situ* variable temperature SPXRD heatmaps for the ZnCl_2 and ZnF_2 reactions, respectively. The analogous ZnBr_2 reaction is shown in the main text (Figure 1). These data were used for sequential Rietveld analysis, which is presented in Figure 4 in the main text.

In situ SPXRD of the $3 \text{ ZnCl}_2 + \text{Li}_6\text{WN}_4$ reaction (Figure S2) proceeds similarly to the ZnBr_2 -based reaction shown in the main text (Figure 1). Bragg peaks arising from the precursors ($3 \text{ ZnCl}_2 + \text{Li}_6\text{WN}_4$) stay steady up to 200 °C, where they begin to decrease in intensity. Simultaneously, Bragg peaks for Zn_3WN_4 , LiCl , and Li_2ZnCl_4 begin to increase in intensity. The set of Bragg peaks corresponding to the Li_2ZnCl_4 phase fade out by 310 °C. We suspect that Li_2ZnCl_4 is not an essential intermediate but rather the product of a transient side reaction between the precursor ZnCl_2 and product LiCl . The intensity of the Bragg peaks corresponding to the LiCl phase reaches a maximum near ca. 340 °C, and then slowly decreases in intensity up to 550 °C (LiCl melting point is 605 °C).^[11] Zn_3WN_4 's Bragg peaks remain approximately constant in intensity above 300 °C, persisting through the duration of the heating process. These processes are consistent with the following reactions:

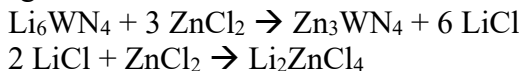


Figure S3 shows that the $3 \text{ ZnF}_2 + \text{Li}_6\text{WN}_4$ reaction does not yield Zn_3WN_4 until 565 °C, a much higher temperature than the ZnCl_2 and ZnBr_2 reactions. Initial reactivity begins near 310 °C, indicated by a decrease in intensities for the set of Bragg peaks corresponding to Li_6WN_4 and ZnF_2 . This initial reactivity is well below the melting point of ZnF_2 (872 °C).^[11] Concurrent with this initial reaction, an unknown phase briefly grows in (between 310 °C and 404 °C). Extrapolating from the ZnBr_2 and ZnCl_2 reactions, the phase is likely a Li-Zn-F intermediate, but ternary fluorides in this space are poorly characterized. Li_2ZnF_4 has been reported, but the structure is not well described and the unit cell does not match the unknown phase. This intensity of the Bragg peaks arising from the intermediate phase decreases to zero by 404 °C, above which Li_6WN_4 is the only crystalline phase up to 565 °C. At this point, Li_6WN_4 fades out and Zn_3WN_4 , LiF , and a rocksalt phase fit with WN grow in. The presence of this rocksalt phase indicates that the higher reaction temperature and greater exothermicity of the ZnF_2 reaction (compared with the Cl and Br versions) leads to a substantial degree of decomposition of the Zn_3WN_4 phase. Therefore, this reaction was not explored further.

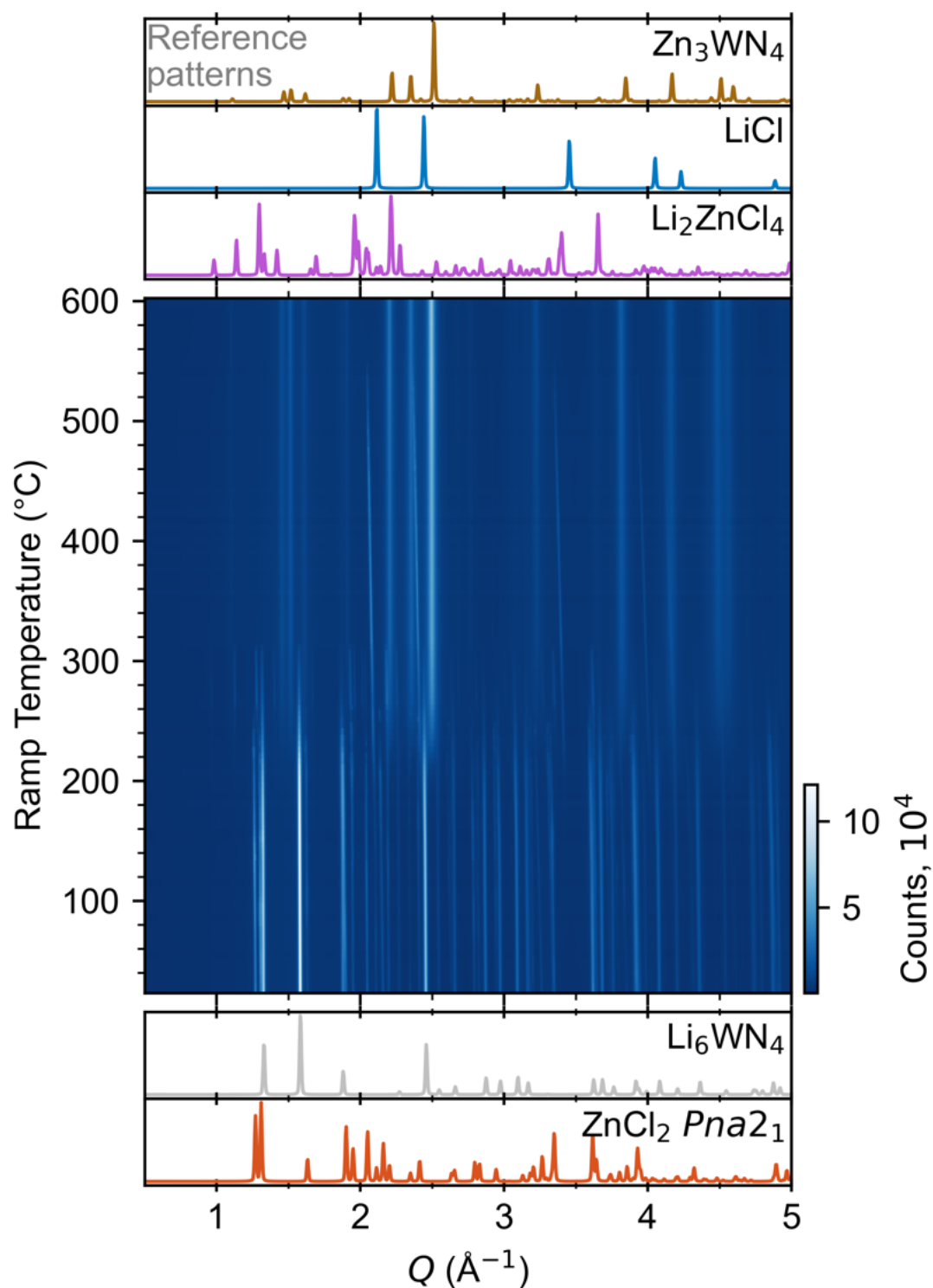


Figure S2. Heatmap of *in situ* SPXRD data upon heating 3 ZnCl_2 + Li_6WN_4 at +10 °C/min. Reference patterns for the reactants and products/intermediates are simulated at the bottom and top, respectively (ICSD Col. Codes 2459 for ZnCl_2 , 66096 for Li_6WN_4 , 402399 for Li_2ZnCl_4 , and 27981 for LiCl).^[1]

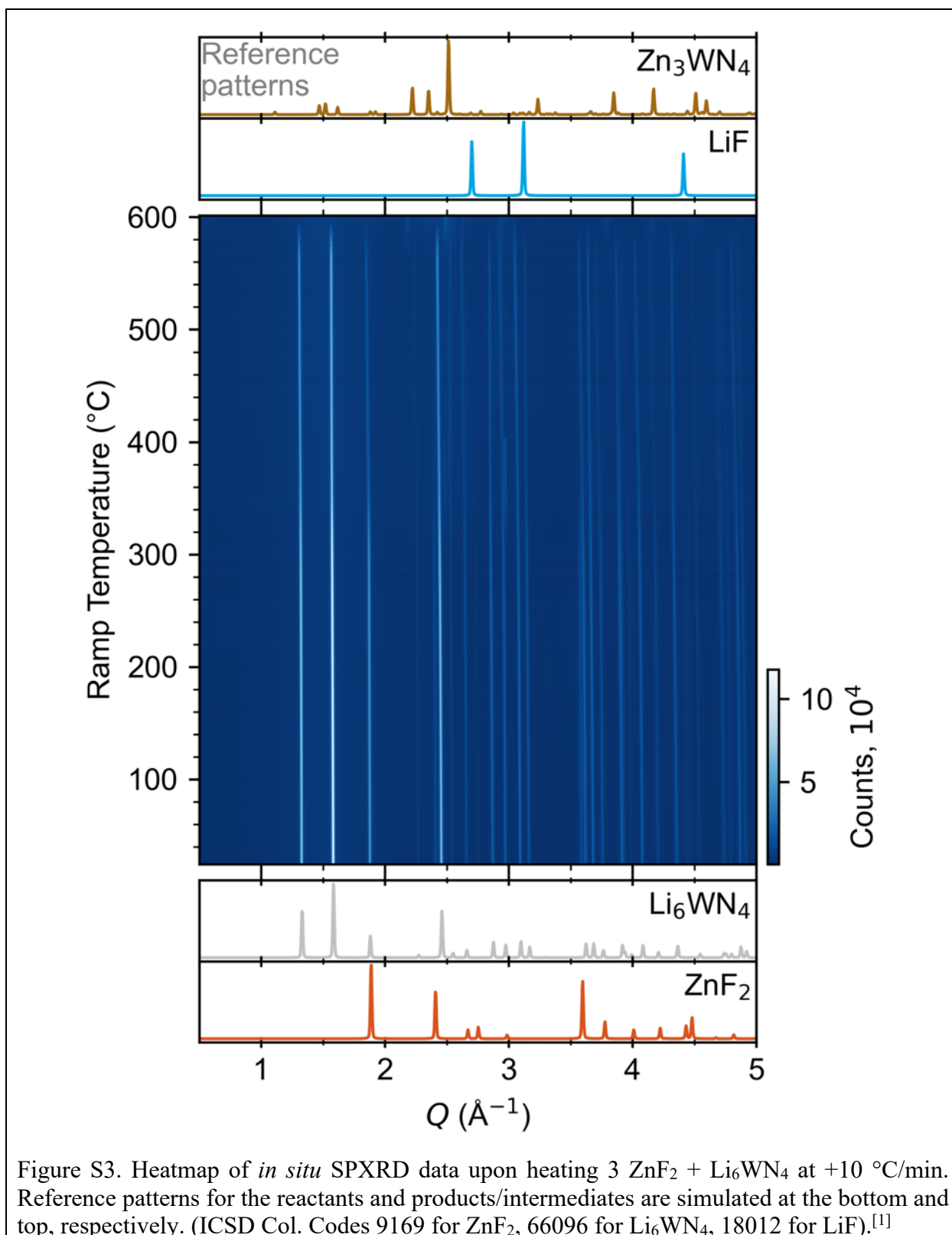


Figure S3. Heatmap of *in situ* SPXRD data upon heating 3 ZnF₂ + Li₆WN₄ at +10 °C/min. Reference patterns for the reactants and products/intermediates are simulated at the bottom and top, respectively. (ICSD Col. Codes 9169 for ZnF₂, 66096 for Li₆WN₄, 18012 for LiF).^[1]

Evidence of decomposition in the $3 \text{ZnCl}_2 + \text{Li}_6\text{WN}_4$ reaction

Figure S4 shows that a trace Zn impurity can be detected in reactions between $\text{Li}_6\text{WN}_4 + 3.1 \text{ZnCl}_2$, even when heated at low temperatures (ca. 250 °C). This impurity makes the powder appear grey in color. The Zn is likely produced via decomposition of Zn_3WN_4 during the highly exothermic reaction (See DSC measurements, Figure 5). Surprisingly, we do not observe W or WN. This may indicate that tungsten remains in the Zn_3WN_4 phase (which would then be Zn-poor), or that the W (or WN) is amorphous.

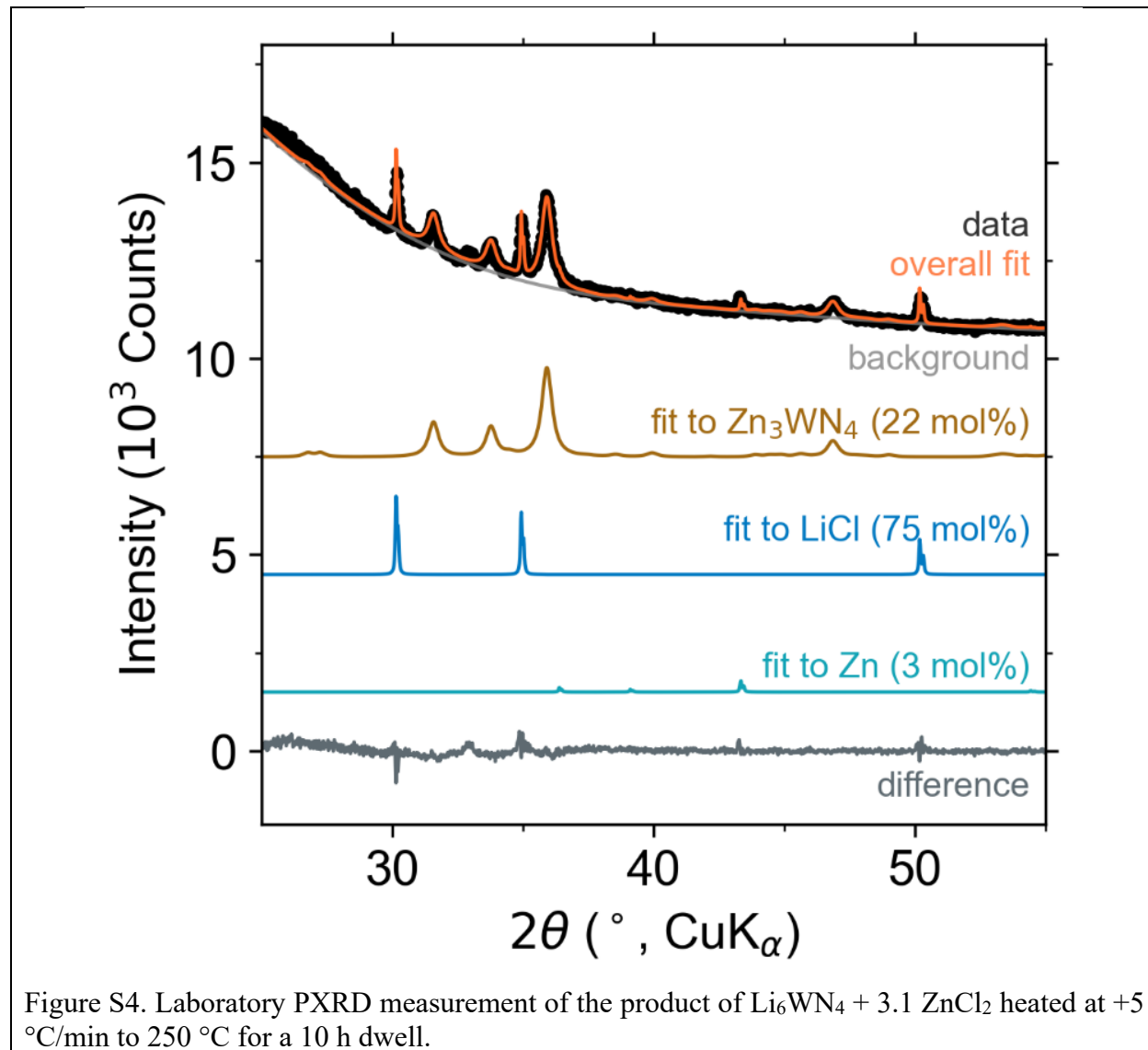


Figure S4. Laboratory PXRD measurement of the product of $\text{Li}_6\text{WN}_4 + 3.1 \text{ZnCl}_2$ heated at +5 °C/min to 250 °C for a 10 h dwell.

Compositional characterization

X-ray Fluorescence (XRF) spectroscopy identified a Zn:W ratio of 3.8:1, in excess of the expected 3:1 ratio for Zn_3WN_4 . XRF was conducted on pelletized powder after washing away the bromide byproduct. The excess zinc may be incorporated in the wurtzite-derived lattice, as suggested by Rietveld analysis (discussed below). A representative raw spectrum is shown in Figure S5. Spectra were collected at 4 different points across the pellet, and each spectrum was fit using the Bruker software to quantify Zn and W atomic ratios. The Zn:W ratio of 3.8:1 was calculated by averaging the Zn:W values from the 4 spectra.

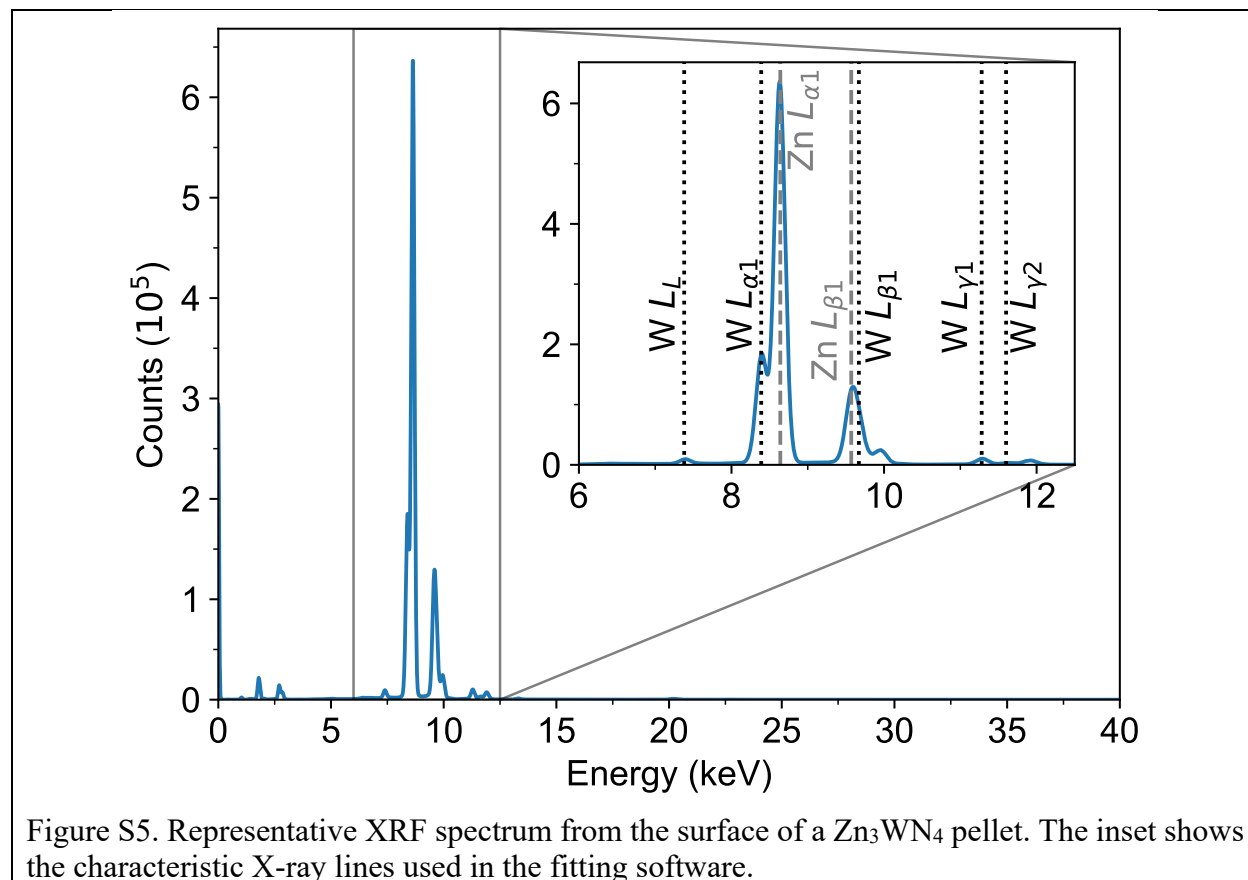


Figure S5. Representative XRF spectrum from the surface of a Zn_3WN_4 pellet. The inset shows the characteristic X-ray lines used in the fitting software.

Structural models for the high resolution SPXRD measurements

The refined lattice parameters for Zn_3WN_4 are shown in Tables S1.

Table S1. Refined atomic coordinates for Zn_3WN_4 in space group $Pmn2_1$ from the SPXRD shown in Figure 1a. The unit cell parameters refined to $a = 6.5602(8)$ Å, $b = 5.6813(7)$ Å, and $c = 5.3235(2)$ Å. $R_{\text{exp}} = 1.182$ %, $R_{\text{wp}} = 3.989$ %, $R_p = 2.802$ %, GOF = 3.374. This structure is shown in Figure 4d.							
Site	Wyckoff	Atom	x	y	z	Occupancy	B_{iso} (Å ²)
Zn1	4b	Zn	0.251(1)	0.834(1)	0.697(1)	1.00(1)	0.10(4)
Zn1	4b	W	0.251(1)	0.834(1)	0.697(1)	0.00(1)	0.10(4)
Zn2	2a	Zn	0	0.337(6)	0.698(1)	1.00(1)	0.20(7)
Zn2	2a	W	0	0.337(6)	0.698(1)	0.00(1)	0.20(7)
W1	2a	W	0	0.670(2)	0.221(1)	0.83(2)	0.44(4)
W1	2a	Zn	0	0.670(2)	0.221(1)	0.17(2)	0.44(4)
N1	4b	N	0.765(2)	0.846(3)	0.095(1)	1	0.30(18)
N2	2a	N	0	0.330(4)	0.116(2)	1	0.4(3)
N3	2a	N	0	0.678(4)	0.555(2)	1	0.4(3)

We considered several structural models of Zn_3WN_4 when conducting Rietveld analysis against our high resolution SPXRD patterns (Table S2). Several terms were allowed to vary for each approach: sample displacement, lattice parameters, size broadening (Lorentzian), strain broadening (Lorentzian), isotropic displacement parameters, and a 15-term background Chebyshev polynomial. Our most robust model was a single-phase model that allowed for a small degree of cation disorder for $Pmn2_1$ Zn_3WN_4 , but with each cation site fixed to full occupancy (e.g., the Zn1 site was refined with Zn occupancy set to $1-x$ and W occupancy x). This model resulted in an R_{wp} of 3.989 % and is shown in Figure 4, Table S1, and Figure S6a. For comparison, a simpler model of $Pmn2_1$ Zn_3WN_4 with fixed cation occupancies (e.g., the Zn1 site fixed with 1.0 Zn occupancy) gave a significantly worse fit to the data ($R_{\text{wp}} = 4.638$ %). Atomic positions were allowed to refine for both these single phase models. However, our diffuse reflectance spectroscopy measurements suggest that the material is not a single homogeneous phase.

Given the two distinct absorption onsets shown in the diffuse reflectance spectrum (Figure 5), we also considered a two-phase model in our Rietveld refinements. For the first two-phase model, we started with the $Pmn2_1$ Zn_3WN_4 from the fixed cation occupancy models. We then fixed atomic positions. Next, we created a model for cation disordered Zn_3WN_4 in a $P6_3mc$ structure (i.e., the wurtzite structure type), and set the lattice parameters to $a = 3.280$ Å and $c = 5.324$ Å such that the (100), (002), and (101) reflections of the $P6_3mc$ structure matched the (210), (002), and (211) reflections, respectively, of the $Pmn2_1$ structure (i.e., $a_{\text{dis}} = 0.5a_{\text{ord}}$ and $c_{\text{dis}} = c_{\text{ord}}$; where “dis” and “ord” indicate the disordered $P6_3mc$ and the ordered $Pmn2_1$ structures, respectively). This structure is consistent with the cation-disordered Zn_3WN_4 synthesized via thin film sputtering.^[13] We then refined the size and strain broadening for both phases. This refinement resulted in 78 mol% phase fraction of $Pmn2_1$, 22 mol% for $P6_3mc$, and an R_{wp} value of 3.953 % (Figure S7a), comparable to the single-phase model.

The best fit was obtained via a two-phase model, but with non-physical lattice parameters. Allowing the $P6_3mc$ lattice parameters to freely refine results in the best fit we obtained by the Rietveld method ($R_{wp} = 3.742\%$). However, the model is likely non-physical. In this model, the refined c lattice parameter for this $P6_3mc$ phase increases substantially ($5.451(2)\text{ \AA}$) compared to the $Pmn2_1$ phase ($c = 5.3228(2)\text{ \AA}$), which is not consistent with prior studies of order-disorder transitions in wurtzite derived structures (e.g., ZnGeN_2).^[14] The c lattice parameters of ZnGeN_2 are identical in the $Pna2_1$ (the ordered structure) and $P6_3mc$ (the disordered structure), because cation disorder does not affect the layer spacing of the hcp anions along the $(00l)$ direction. This analysis reveals ambiguities in these two-phase models.

Given the limitations of the two-phase models, we posit that the single phase model provides the most reliable fit to the SPXRD data without over-fitting the pattern.^[15] Yet, the SPXRD measurements probe the long range average ordered structure. Local ordering—which we do not probe here—may influence the optical absorption properties shown in Figure 5. The impact of local ordering on optical properties has been characterized in the halide perovskite CsSnBr_3 ,^[16] in Fe doped SrTiO_3 ,^[17] and in carbon coated FeF_3 .^[18]

Table S2. Summary of models considered for the high resolution SPXRD data for Zn_3WN_4 .

Rietveld approach	Space group	Composition	$R_{wp}(\%)$	Figure
Single phase. Refined cation occ.	$Pmn2_1$	$\text{Zn}_{3.17}\text{W}_{0.83}\text{N}_4$	3.989	1a and S6a
Single phase. Fixed cation occ.	$Pmn2_1$	Zn_3WN_4	4.638	S6b
Two phases. Fixed cation occ.	$Pmn2_1$	Zn_3WN_4	3.953	S7a
Fixed a and c for $P6_3mc$	$P6_3mc$	$\text{Zn}_{0.75}\text{W}_{0.25}\text{N}$		
Two phases. Fixed cation occ.	$Pmn2_1$	Zn_3WN_4	3.742	S7b
Refined a and c for $P6_3mc$	$P6_3mc$	$\text{Zn}_{0.75}\text{W}_{0.25}\text{N}$		

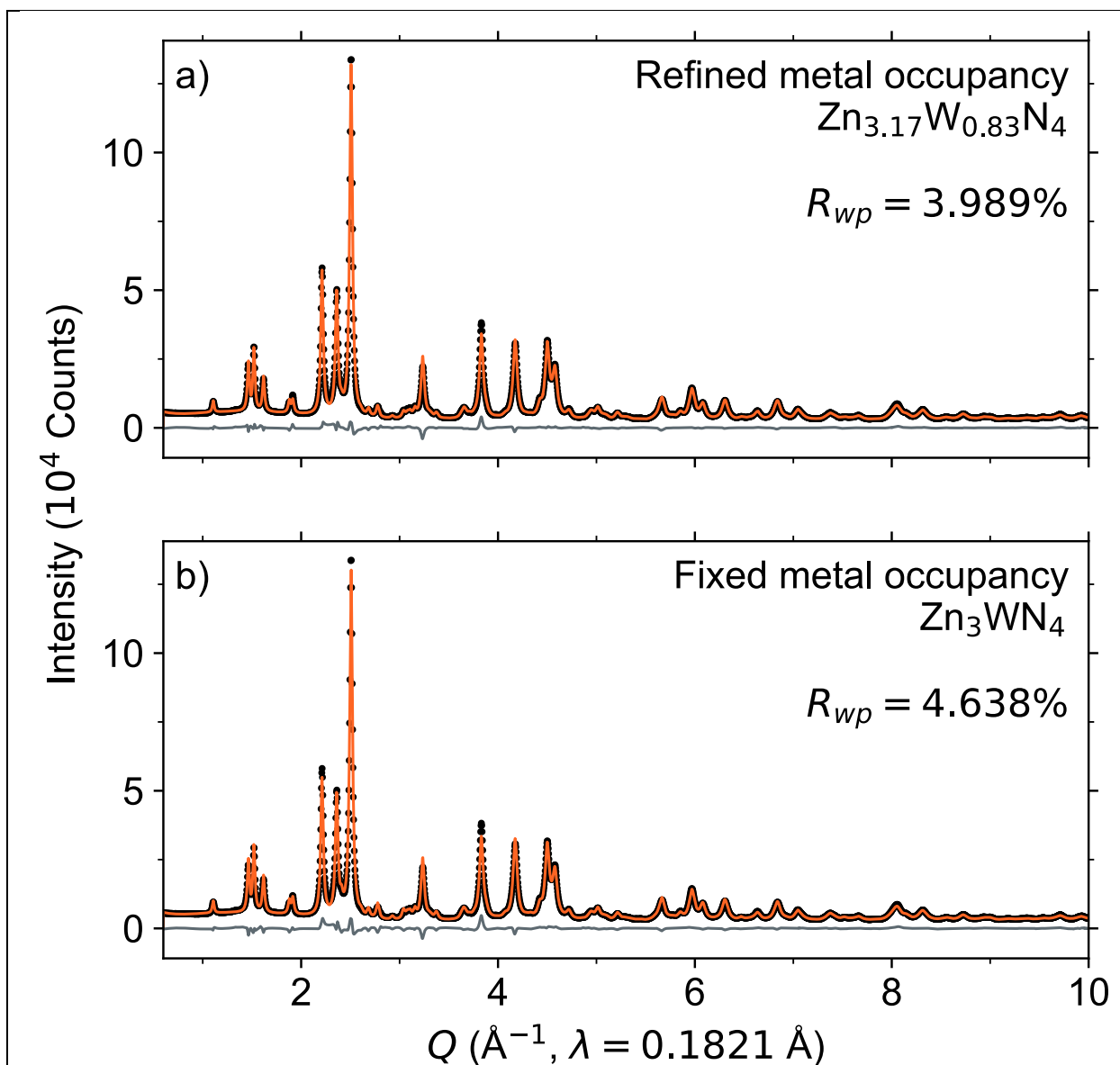


Figure S6. The high resolution SPXRD measurement of the Zn_3WN_4 sample fit with single-component models of $Pmn2_1$ with a) the occupancies of the metal sites refined to $\text{Zn}_{3.17}\text{W}_{0.83}\text{N}_4$ (also shown in Figure 4), and b) fixed metal site occupancy at cation-ordered Zn_3WN_4 .

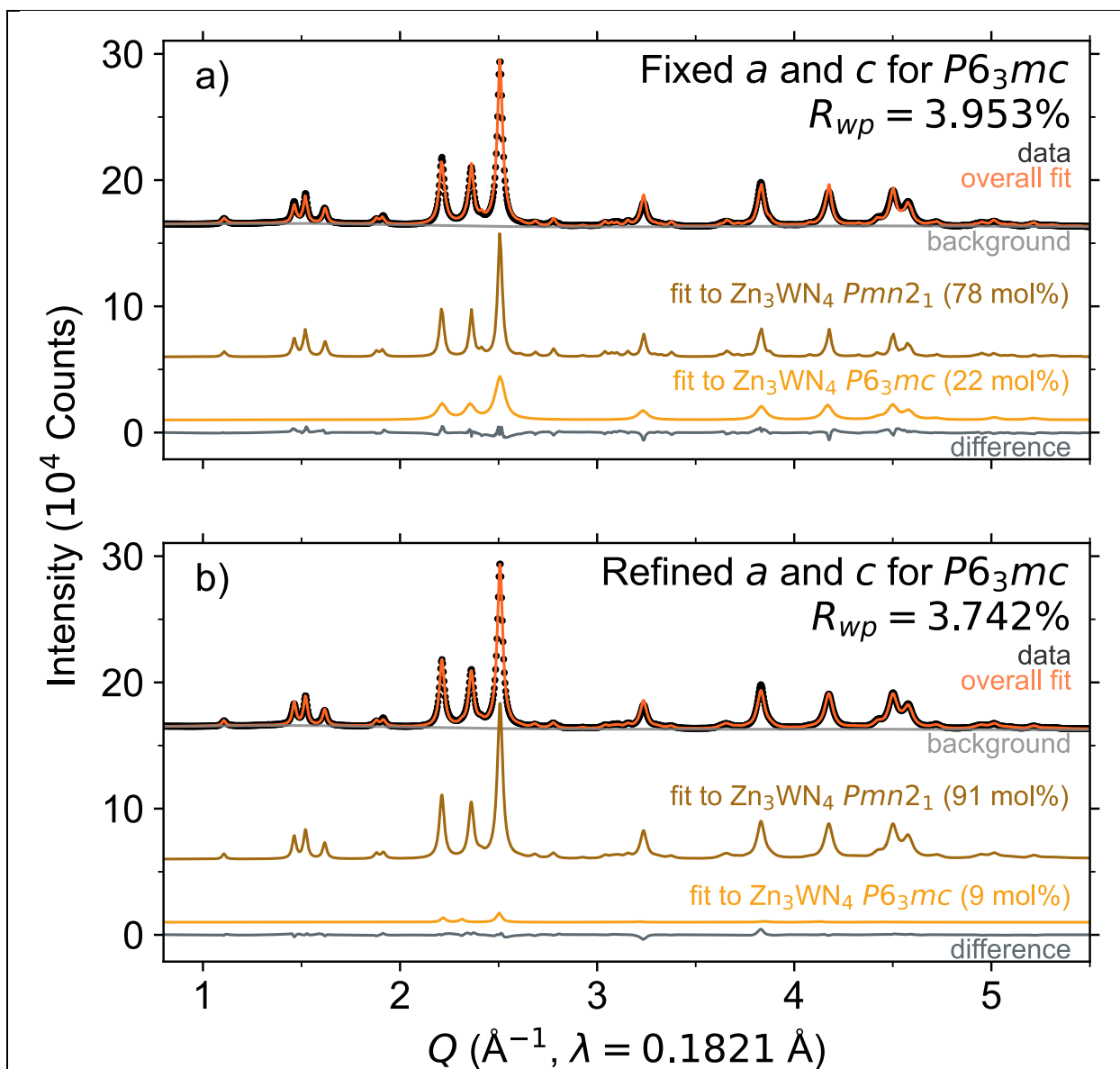
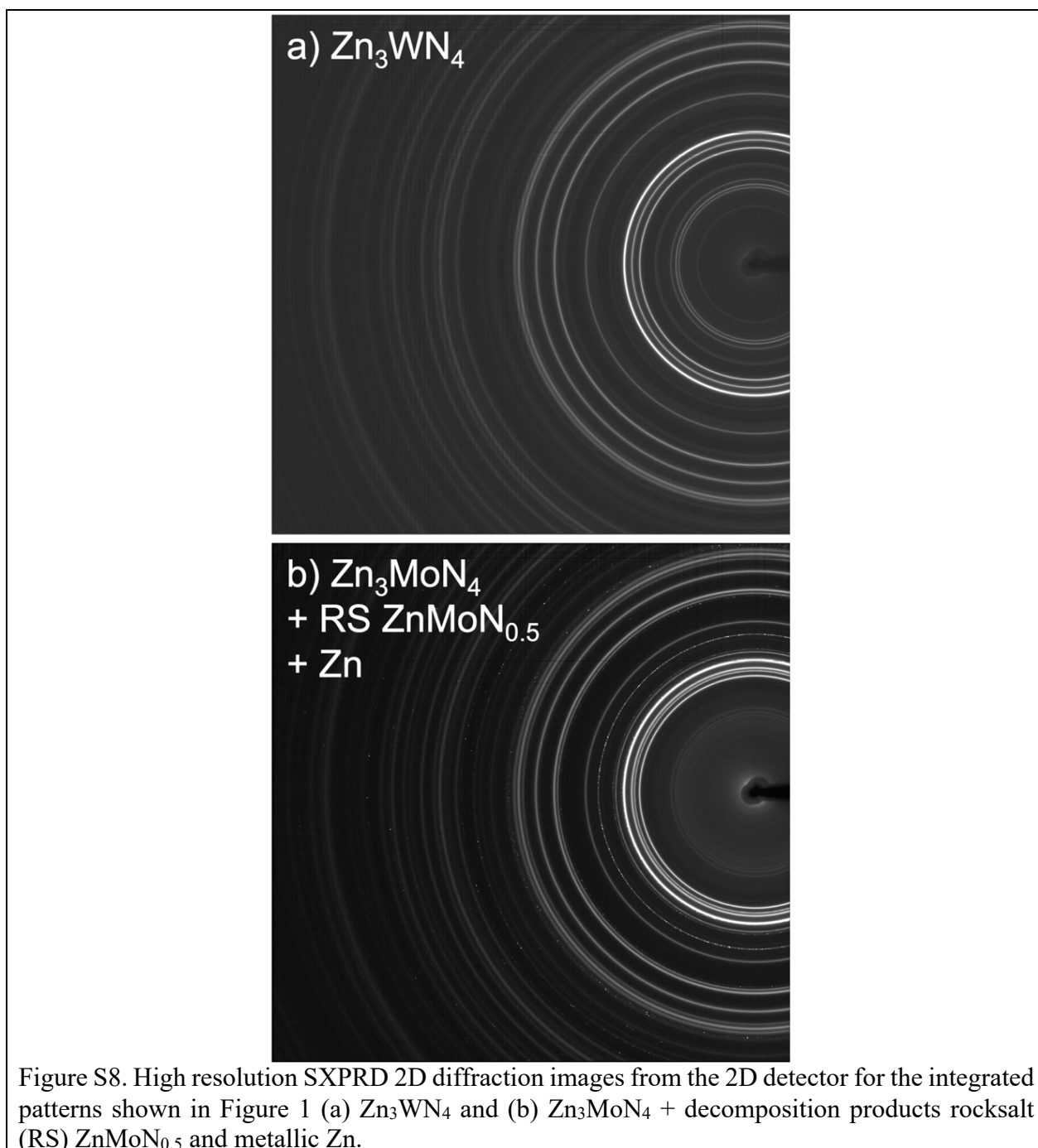


Figure S7. Rietveld refinement of the high-resolution SPXRD data of Zn_3WN_4 using a two-component model with a) the $P6_3mc$ lattice parameters fixed relative to the $Pmn2_1$ values and b) the $P6_3mc$ lattice parameters freely refined.



Qualitative inspection of the 2D diffraction images show that the diffraction rings for the Zn_3WN_4 powder are homogeneous (Figure S8). If rings with two different morphologies were present, this would suggest the presence of two distinct phases with different crystallinity, size, and strain. That we see only one morphology of ring in the 2D detector image supports either a single phase or multiple phases with nearly identical crystallinity, size, and strain. In our Rietveld refinement that modeled the data using two phases, the fit to the data is significantly worse when we constrain the size and strain broadening terms to be the same for both phases. These findings support our use of the single-phase model.

Magnetic susceptibility measurements

Magnetic measurements were performed on Zn_3WN_4 using a Quantum Design Physical Property Measurement System (PPMS). A powder sample of Zn_3WN_4 was loaded into a small packet (0.001125 mg) and secured inside a plastic straw for the measurement. Magnetic susceptibility (χ) of Zn_3WN_4 was measured as a function of temperature shows largely diamagnetic behavior with a trace paramagnetic impurity (Figure S9a). Similarly, magnetization (M) as a function of applied field (H) at 2 K shows that diamagnetism dominates the field-dependent magnetization (Figure S9b). These findings are inconsistent with pure Zn_3WN_4 , which should be purely diamagnetic. Zn impurities, if present, would also give a diamagnetic response. The paramagnetic component suggests the possibility of a reduced tungsten species (e.g., W^{5+}), possibly as a sub-nitride (e.g., $\text{Zn}_3\text{WN}_{4-\delta}$), an oxynitride impurity (e.g., $\text{Zn}_3\text{WN}_{4-x}\text{O}_x$), or a W-rich phase (e.g., $\text{Zn}_{3-\delta}\text{W}_{1+\delta}\text{N}_4$).

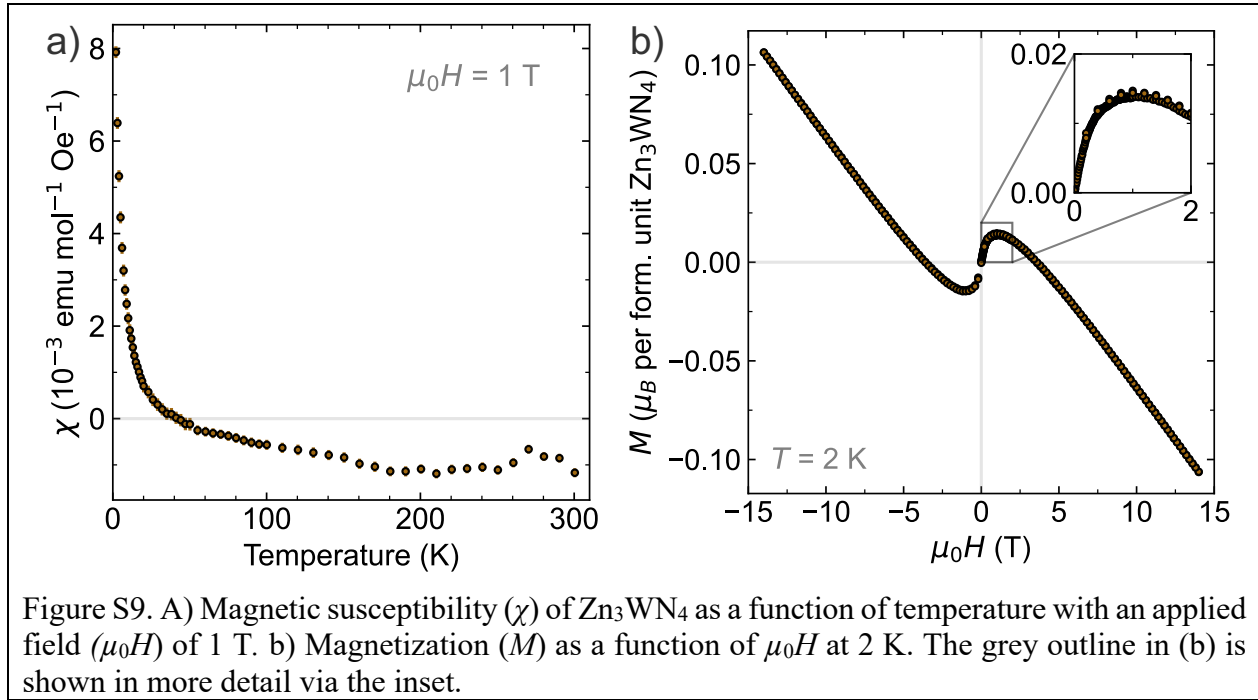
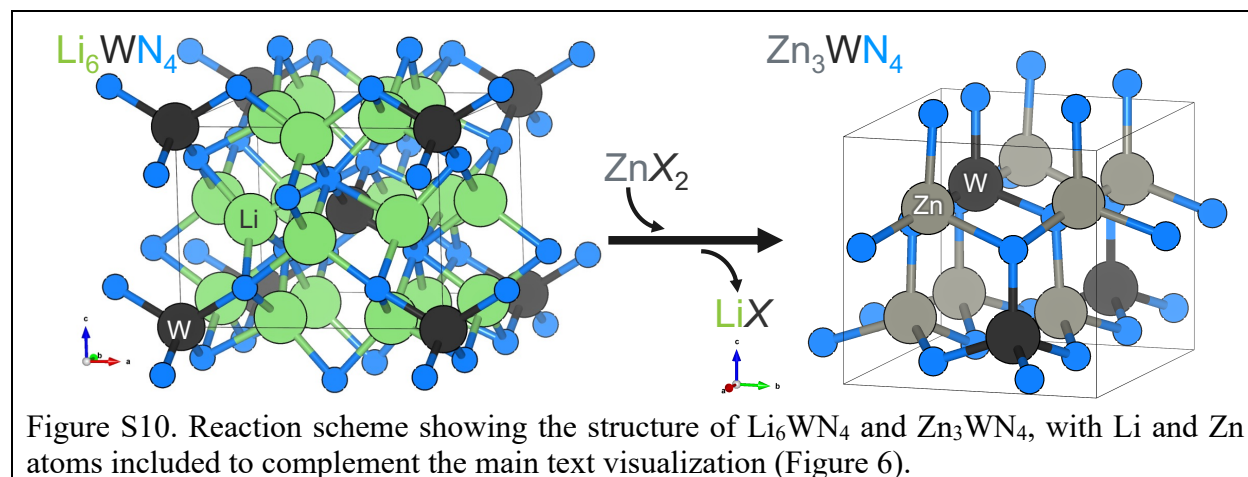


Figure S9. A) Magnetic susceptibility (χ) of Zn_3WN_4 as a function of temperature with an applied field ($\mu_0 H$) of 1 T. b) Magnetization (M) as a function of $\mu_0 H$ at 2 K. The grey outline in (b) is shown in more detail via the inset.

Full structure visualizations of Li_6WN_4 and Zn_3WN_4



Synthesis of Zn_3MoN_4

The synthesis strategy used for Zn_3WN_4 was also applied to synthesize Zn_3MoN_4 , but the product exhibited partial decomposition. Analysis of the SPXRD pattern collected for the Mo analog of Li_6WN_4 , synthesized via the reaction $\text{Li}_6\text{MoN}_4 + 3 \text{ZnBr}_2 \rightarrow \text{Zn}_3\text{MoN}_4 + 6 \text{LiBr}$, suggests phase decomposition (Figure S11). In addition to the desired Zn_3MoN_4 (56 mol%), Rietveld analysis of High resolution SPXRD data show that a rocksalt (RS) structure fit as $\text{ZnMoN}_{0.5}$ also forms (23 mol%), along with a Zn impurity (20 mol%). This RS phase exhibits a substantially larger lattice parameter ($a = 4.7106(3) \text{ \AA}$) than the defect-RS phase Mo_2N ($a = 4.16 \text{ \AA}$ to 4.19 \AA).^[19,20] Therefore, we hypothesize it may be a $(\text{Zn},\text{Mo})\text{N}_x$ material, as octahedral Zn^{2+} has a substantially larger ionic radius (0.74 \AA) than octahedral Mo^{x+} (0.65 \AA for Mo^{4+} , 0.69 \AA for Mo^{3+}).^[21] The rocksalt $\text{ZnMoN}_{0.5}$ phase was created from a $Fm\bar{3}m$ Mo_2N starting model. Rietveld analysis with the composition of $\text{ZnMoN}_{0.5}$ provides a reasonable fit. Further analysis of this material is beyond the scope of this manuscript. Additional minor peaks that we have not indexed are present (possibly higher order oxides). These impurity phases suggest that Zn_3MoN_4 is less stable at elevated temperatures than Zn_3WN_4 . This decomposition occurs despite the excess ZnBr_2 which was intended to serve as a heat sink during the exothermic reaction. Despite the partial decomposition of the phase, Zn_3MoN_4 is still the major phase in the pattern. As with Zn_3WN_4 , the SPXRD pattern for Zn_3MoN_4 shows evidence of cation-ordering in the form of the $Pmn2_1$ reflections at low angle: e.g., (010), (110), (101), (011). However, these reflections are weaker than in the W case, owing to the lower scattering factor of Mo compared to W. We focused our work on Zn_3WN_4 because W scatters X-rays more strongly than Mo (facilitating characterization) and because our Zn_3WN_4 products exhibited higher phase purity.

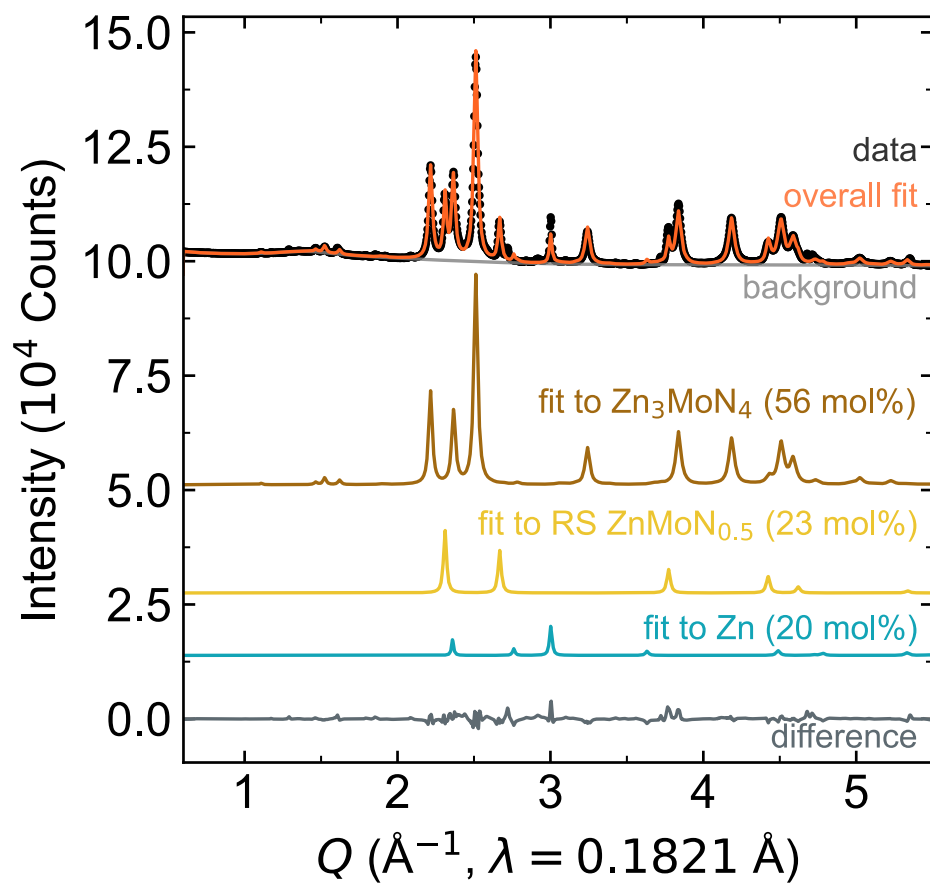


Figure S11. SPXRD pattern and Rietveld refinement of the washed products from the reaction between $\text{Li}_6\text{MoN}_4 + 4.2 \text{ ZnBr}_2$ (excess ZnBr_2).

References

- [1] W. X. Yuan, J. W. Hu, Y. T. Song, W. J. Wang, Y. P. Xu, *Powder Diffr.* **2005**, *20*, 18–21.
- [2] D. B. G. Williams, M. Lawton, *J. Org. Chem.* **2010**, *75*, 8351–8354.
- [3] P. J. Chupas, K. W. Chapman, C. Kurtz, J. C. Hanson, P. L. Lee, C. P. Grey, *J. Appl. Crystallogr.* **2008**, *41*, 822–824.
- [4] A. A. Coelho, *J. Appl. Crystallogr.* **2018**, *51*, 210–218.
- [5] P. K. Todd, A. M. M. Smith, J. R. Neilson, *Inorg. Chem.* **2019**, *58*, 15166–15174.
- [6] C. Prescher, V. B. Prakapenka, *High Press. Res.* **2015**, *35*, 223–230.
- [7] E. Arca, S. Lany, J. D. Perkins, C. Bartel, J. Mangum, W. Sun, A. Holder, G. Ceder, B. Gorman, G. Teeter, W. Tumas, A. Zakutayev, *J. Am. Chem. Soc.* **2018**, *140*, 4293–4301.
- [8] K. Momma, F. Izumi, *J. Appl. Crystallogr.* **2011**, *44*, 1272–1276.
- [9] A. Jain, G. Hautier, S. P. Ong, C. J. Moore, C. C. Fischer, K. A. Persson, G. Ceder, *Phys. Rev. B* **2011**, *84*, 045115.
- [10] A. Jain, S. P. Ong, G. Hautier, W. Chen, W. D. Richards, S. Dacek, S. Cholia, D. Gunter, D. Skinner, G. Ceder, K. A. Persson, *APL Mater.* **2013**, *1*, 011002.
- [11] J. R. Rumble (ed.), “Bond Dissociation Energies in Diatomic Molecules” in *CRC Handbook of Chemistry and Physics*, CRC Press/Taylor & Francis, Boca Raton, FL., **n.d.**
- [12] C. Martin, A. Durif-Varambon, J.-C. Joubert, *Bull. Minéralogie* **1965**, *88*, 141–141.
- [13] W. Sun, C. J. Bartel, E. Arca, S. R. Bauers, B. Matthews, B. Orvañanos, B.-R. Chen, M. F. Toney, L. T. Schelhas, W. Tumas, J. Tate, A. Zakutayev, S. Lany, A. M. Holder, G. Ceder, *Nat. Mater.* **2019**, *18*, 732–739.
- [14] E. W. Blanton, K. He, J. Shan, K. Kash, *J. Cryst. Growth* **2017**, *461*, 38–45.
- [15] B. H. Toby, *Powder Diffr.* **2006**, *21*, 67–70.
- [16] D. H. Fabini, G. Laurita, J. S. Bechtel, C. C. Stoumpos, H. A. Evans, A. G. Kontos, Y. S. Raptis, P. Falaras, A. Van der Ven, M. G. Kanatzidis, R. Seshadri, *J. Am. Chem. Soc.* **2016**, *138*, 11820–11832.
- [17] H. A. J. L. Mourão, O. F. Lopes, W. Avansi, M. J. M. Pires, S. Souza, C. Ribeiro, V. R. Mastelaro, *Mater. Sci. Semicond. Process.* **2017**, *68*, 140–146.
- [18] N. Yamakawa, M. Jiang, B. Key, C. P. Grey, *J. Am. Chem. Soc.* **2009**, *131*, 10525–10536.
- [19] C. L. Bull, T. Kawashima, P. F. McMillan, D. Machon, O. Shebanova, D. Daisenberger, E. Soignard, E. Takayama-Muromachi, L. C. Chapon, *J. Solid State Chem.* **2006**, *179*, 1762–1767.
- [20] B. Cao, J. C. Neufeind, R. R. Adzic, P. G. Khalifah, *Inorg. Chem.* **2015**, *54*, 2128–2136.
- [21] R. D. Shannon, *Acta Crystallogr. Sect. A* **1976**, *32*, 751–767.